CHAPTER 4

DNA/protein binding and molecular docking studies of two tetranuclear Cu(II) complexes with double-open-cubane core like structure

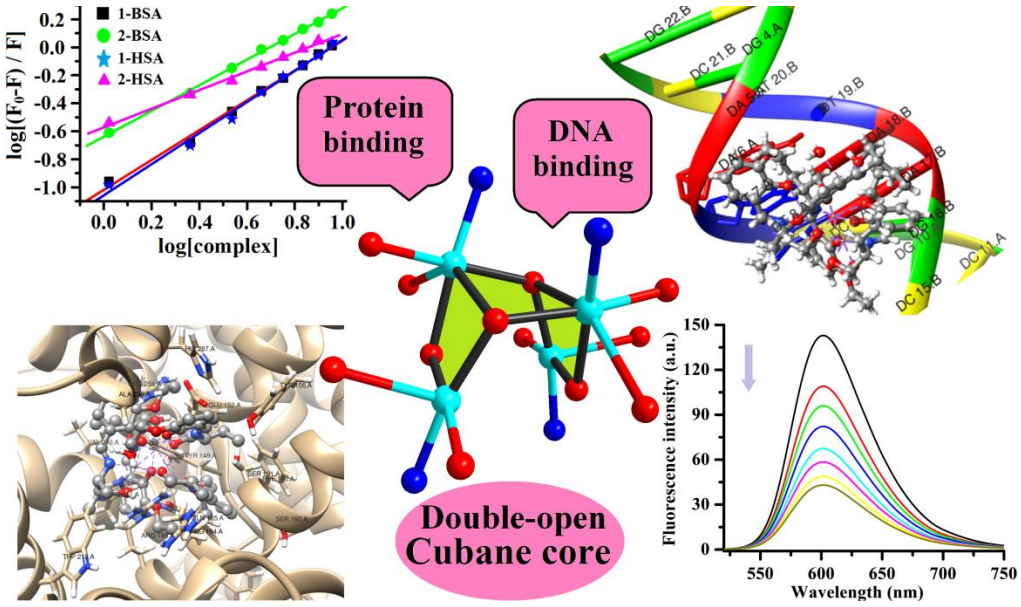

A. Paul et al., Inorganic Chimica Acta, under revision.

4.1 Introduction

The chemistry of polynuclear Cu(II) clusters has received increasing interest because of their structural diversity and potential applications in molecular magnetism [4.1] and in the area of biochemistry [4.2]. Multinuclear copper compounds with various structures and compositions [4.3a-4.3i] are reported in the literature with their potential applications in the field of magnetism [4.4], catalysis [4.5] and molecular biology [4.6]. Cu(II) complexes are also used as Among the polynuclear copper(II) complexes, tetranuclear copper cubane are draw special attention for their structural points of view. Various cubane geometries are reported in the literature for example regular [4.7], single open [4.8], double open [4.9] and face sharing dicubane [4.9b, 4.10].

Lots of copper(II) complexes are used as metallo-pharmaceuticals [4.11] and shows antimicrobial [4.12], antifungal [4.13], antibacterial [4.14], antitumoral [4.15], antiviral [4.16], antipyretic [4.13a] and antidiabetic activities [4.17].

Several studies show that the DNA is the primary intracellular target of antitumor / anti-cancer drugs, and due to the DNA binding / cleaving ability of drugs they can induce apoptosis in cancer cells [4.18]. As a result, the complexes which can able to bind and cleave DNA under physiological conditions may be act as drugs [4.19, 4.20].

To understand the potential of metal complexes as drugs, studies on the binding behavior of metal complexes with serum albumins is a vital step since it has a direct effect on therapeutic efficiency of the complexes [4.21]. Hence, the activity of metal complexes towards DNA and serum albumins are important to serve as drugs.

Our recent studies have been focused on the interaction of Schiff base metal complexes with nucleic acid (CT-DNA) and serum albumins (BSA and HSA). In the present contribution, we report the synthesis, crystal structure and interactions of two tetranuclear copper(II) complexes,

$[Cu_4(L)_2(HL)_2(H_2O)_2](pv)_2$ (**1**) and $[Cu_4(L)_2(HL)_2(H_2O)_2](ssal)$ (**2**) with CT-DNA and serum albumins. Mode of interactions of complexes with CT-DNA / serum albumins has also been explored by molecular docking studies.

4.2 Experimental

4.2.1 Materials and physical measurments

Highly pure 3-ethoxy salicylaldehyde, 2-amino-1-butanol, bovine serum albumin (BSA), human serum albumin (HSA), calf thymus DNA (CT-DNA), and ethidium bromide (EB) were purchased from Aldrich Chemical Co. Inc. and used as received. Other chemicals used were of analytical grade. Solvents were purifies and dried by standard procedures [4.22] before used for spectroscopic studies.

Elemental analyses (carbon, hydrogen and nitrogen) were performed using a Perkin-Elmer 240C elemental analyzer. IR spectra were recorded (as KBr pellets) on a Bruker Vector 22FT IR spectrophotometer operating from 400 to 4000 cm^{-1}. NMR spectra of ligand recorded on Bruker 400 MHz instrument. UV-vis absorption spectra were measured on a Shimadzu UV-1601 UV-vis spectrophotometer at room temperature using matched quartz cuvettes (1.0 cm path length and a 3 cm^3 volume) were used for all measurements. Emission spectra were recorded on a Hitachi F-7000 spectrofluorimeter. Room temperature (300 K) spectra were obtained in methanolic solution using a quartz cell of 1 cm path length. The slit width was 5 nm for both excitation and emission.

The fluorescence quantum yield was determined using phenol as a reference and methanol medium for both complexes and reference. Emission spectra were recorded by exciting the complex and the reference phenol at the same wavelength, maintaining nearly equal absorbance

(~ 0.1). The area of the emission spectrum was integrated using the software available in the instrument and the quantum yield calculated [4.23] according to the following equation:

$$\Phi_s = \Phi_r \frac{A_s}{A_r} \frac{I_r}{I_s} \frac{\eta_s^2}{\eta_r^2}$$

Where Φ_s and Φ_r are the fluorescence quantum yield of the sample and reference, respectively. A_s and A_r are the respective optical densities at the wavelength of excitation, I_s and I_r correspond to the areas under the fluorescence curve; and η_s and η_r are the refractive index values for the sample and reference, respectively. The fluorescence enhancement efficiency (%) was calculated by using equation $[(F - F_o)/F_o] \cdot 100$ and the corresponding quenching efficiency (%) by $[(F_o - F)/F_o] \cdot 100$, where F_0 and F are the maximum fluorescence intensity of the complex before exposure and in presence of the analyte, respectively.

4.2.2 X-ray crystallography

The crystal data of complexes were collected using a Nonius Kappa CCD diffractometer with graphite monochromated Mo-Kα radiation at room temperature. The data set was integrated with the Denzo-SMN package [4.24] and corrected for Lorentz, polarization and absorption effects (SORTAV) [4.25]. The structures were solved by direct methods using SIR97 [4.26] system of programs and were refined using full-matrix least-squares with all non-hydrogen atoms anisotropically and hydrogens included on calculated positions, riding on their carrier atoms, except the hydrogen atoms forming H-bonds which were refined isotropically. Packing diagrams were done with graphical program Diamond [4.27]. The crystal data and details of the structure refinements are given in Table 4.1. The cif file CCDC numbers are 1909238-1909239 for **1** and **2**, respectively.

Table 4.1 Crystal data and details of structure refinement of complexes

Complex	**1**	**2**
Empirical formula	$C_{62}H_{92}Cu_4N_4O_{18}$	$C_{59}H_{78}Cu_4N_4O_{20}S$
Formula mass, g mol^{-1}	1435.56	1449.47
Crystal system	Orthorhombic	Monoclinic
Space group	*Pbca (No. 61)*	*P21/c (No. 14)*
a, Å	19.0695(4)	16.6529(4)
b, Å	21.6230(4)	17.9750(5)
c, Å	33.7271(9)	22.7586(4)
α, deg	90	90
β, deg	90	110.3960(12)
γ, deg	90	90
V, $Å^3$	13907.0(5)	6385.4(3)
Z	8	4
$D_{(calcd)}$, g cm^{-3}	1.371	1.508
μ(Mo-Kα), mm^{-1}	1.274	1.422
F(000)	6016	3008
Theta range, deg	2.1, 25.0	2.6, 28.0
No. of collected data	22552	54028
No. of unique data	12071	15374
R_{int}	0.061	0.058
Observed reflns [$I > 2\sigma(I)$]	6241	10587
Goodness of fit (F^2)	1.033	1.055
Parameters refined	12071, 775	15374, 817
*R*1, *wR*2 ($I > 2\sigma(I)$) [a]	0.0724, 0.2139	0.0570, 0.1819
Residuals, e $Å^{-3}$	-0.50, 0.59	-0.95, 1.03

[a] $R1(Fo) = \Sigma \big| |Fo| - |Fc| \big| / \Sigma |Fo|$, $wR2(Fo^2) = [\Sigma w (Fo^2 - Fc^2)^2 / \Sigma w (Fo^2)^2]^{½}$

4.2.3 Synthesis of ligand

Multi-dentate Schiff base ligand 2-Ethoxy-6-[(1-hydroxymethyl-propylimino)-methyl]-phenol (H_2L) was prepared by refluxing 1:1 mixture of 2-aminobutanol and 2-hydroxy-3-ethoxybenzaldehyde (Scheme 4.1) in methanol according to the Chapter-3.

4.2.4 Synthesis of complexes

Caution! Metal perchlorate salts in presence of organic ligands are potentially explosive. Only a small amount of material should be prepared, and it should be handled with care.

The complexes have been synthesized by adopting the procedures schematically given in Scheme 4.1.

Scheme 4.1 Synthesis of ligand and complexes

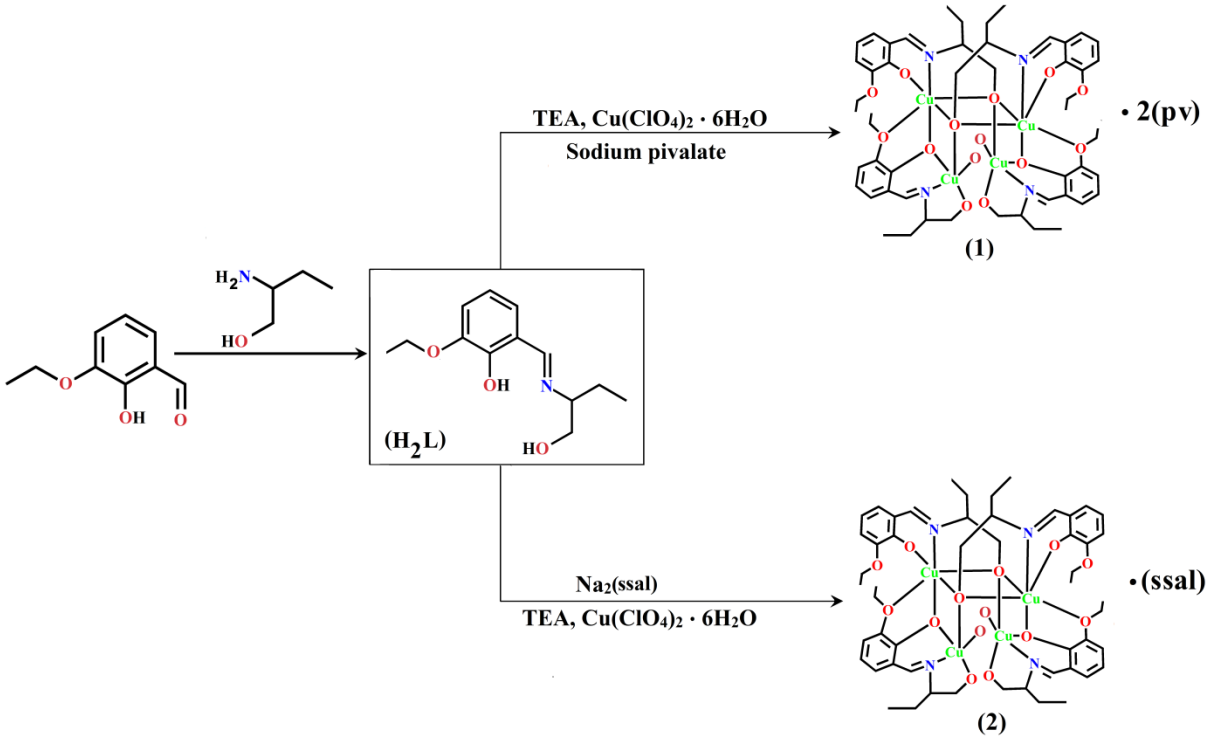

Synthesis of [Cu$_4$(L)$_2$(HL)$_2$(H$_2$O)$_2$]·2(pv) (1)

A methanolic solution (5 mL) of Et_3N (1 mmol) was added drop wise to a methanolic solution (15 mL) of H_2L (1 mmol, 0.237 g) with continuous stirring. The dropwise addition of copper perchlorate hexahydrate (1 mmol; 0.37 g) solution (10 mL in methanol) to this resulting mixture, results a deep green solution. The entire reaction mixture was stirred for 2 hours and then a mixture of methanol-water (1:1) solution (5 mL) of sodium pivalate (Na(pv)) (2 mmol, 0.248 g) was added. Finally the reaction mixture stirred for additional 1 hour, and filtered. X-ray diffraction quality green single crystals were obtained by slow evaporation of solution after a few days. Yield: 83%. Anal. calc. for $C_{62}H_{92}Cu_4N_4O_{18}$ (1435.56): C, 51.87; H, 6.45; N, 3.90 %.

Found: C, 51.23; H, 6.47; N, 3.96 (%). IR (cm^{-1}): 3519 (w), 3470 (w), 2970 (w), 2931 (vw), 2878 (w), 1627 (vs), 1602 (s), 1541 (s), 1436 (vs), 1394 (w), 1362 (w), 1330 (vw), 1293 (w), 1274 (w), 1243 (s), 1213 (vs), 1177 (vw), 1104 (w), 1074 (s), 1010 (s), 943 (s), 897 (s), 849 (w), 785 (s), 734 (vs), 621 (vw).

Synthesis of $[Cu_4(L)_2(HL)_2(H_2O)_2]\cdot(ssal)$ (2)

Complex **2** was synthesized by following the same procedure as adopted for **1**, except using disodium sulfosalicylate ($Na_2(ssal)$) (1 mmol, 0.262 g) in place of sodium pivalate. Yield: 86%. Anal. calc. for $C_{59}H_{78}Cu_4N_4O_{20}S$ (1449.47): C, 48.89; H, 5.42; N, 3.86 %. Found: C, 48.45; H, 5.49; N, 3.93 (%). IR (cm^{-1}): 3481 (vw), 2980 (vw), 2932 (vw), 1627 (vs), 1600 (vs), 1544 (s), 1441 (vs), 1397 (vs), 1328 (s), 1312 (s), 1287 (s), 1241 (vs), 1213 (vs), 1168 (s), 1144 (w), 1110 (w), 1071 (s), 1020 (s), 937 (w), 889 (w), 842 (vw), 830 (w), 783 (w), 740 (vs), 667 (s).

4.2.5 Albumin binding studies

Stock solutions of serum albumins (SAs) were prepared in HEPES buffer (pH 7.2), while the stock solutions of **1** and **2** were prepared by dissolving these in H_2O. Electronic absorption spectral titration were performed by maintaining the constant concentration of serum albumin (334 µM for HSA; 492 µM for BSA) and changing the concentration (0 to 9.02 µM) of Cu(II) complexes. The binding behavior of complexes **1** and **2** with SAs (BSA/HSA) were studied using standard tryptophan fluorescence (λ_{ex} = 280 nm, λ_{em} = 340 nm). Gradual addition of complex solutions (10 µL, 0.3475 mmol) to the solutions of SAs (pH 7.2), results gradual quenching of fluorescence at 340 nm (λ_{ex}, 280 nm) for BSA, and 330 nm (λ_{ex}, 280 nm) for HSA. The Stern-Volmer constant (K_{sv}) and quenching rate constant (k_q) were evaluated using the equations $F_0/F = 1 + K_{sv}$ [complex] and $K_{sv} = k_q\tau_0$ (where F_0 and F are the emission intensities in absence and in presence of the complex, and τ_0 (~ 5×10^{-9} s) is the lifetime of SAs [4.28]. The

binding constant (K_{bin}) and the number of binding sites (n) are calculated using the following Scatchard equation [4.29]:

$$\log[(F_o – F)/F] = \log K_{bin} + n \log[\text{complex}]$$

4.2.6 DNA binding studies

Electronic absorption spectral study

The binding of complexes **1** and **2** with CT-DNA was studied by using electronic absorbance spectroscopic technique. UV-vis absorption spectral titration, the absorption spectra of complexes (5 µM) were recorded with gradual addition of CT-DNA (0 to 30 µM) solution. Intrinsic binding constant (K_{ib}) of the complexes were determined using the following equation [4.30]

$$\frac{[\text{DNA}]}{(\varepsilon_a - \varepsilon_f)} = \frac{[\text{DNA}]}{(\varepsilon_b - \varepsilon_f)} + \frac{1}{K_{ib}(\varepsilon_b - \varepsilon_f)}$$

where [DNA] is the CT-DNA concentration, ε_a is the extinction co-efficient value of the complex at a particular concentration of CT-DNA, ε_f and ε_b are the extinction co-efficient of the complex, in free solution and when it totally bound to CT-DNA, respectively. The plot of [DNA]/($\varepsilon_a - \varepsilon_f$) vs [DNA] gives a straight line with $\frac{1}{(\varepsilon_b - \varepsilon_f)}$ and $\frac{1}{K_{ib}(\varepsilon_b - \varepsilon_f)}$ as slope and intercept, respectively. K_{ib} was calculated from the ratio of the slope to the intercept.

Competitive binding fluorescence measurement

The ethidium bromide displacement studies of complexes were performed with the emission spectroscopy to observe whether the complexes can displace EB from the EB bounded CT-DNA. EB shows strong emission (λ_{ex} = 500 nm, λ_{em} = 602 nm) enhancement in presence of CT-DNA, because of its intercalative binding to CT-DNA. Competitive binding of complexes

with CT-DNA results quenching fluorescence because of displacement of EB from CT-DNA. The Stern-Volmer constant (K_{sv}) was calculated using Stern-Volmer equation [4.23]

$$F_0/F = 1 + K_{sv}[complex]$$

where F_0 and F are the emission intensity in absence and in presence of copper (II) complexes, K_{sv} is the Stern-Volmer constant, and [complex] is the concentration of complex.

4.2.7 Molecular docking

DNA-complex docking

HEX 6.3 program has been used to study the DNA-complex interaction. B-DNA dodecamer $d(CGCGAATTCGCG)_2$ (PDB ID: 1bna) (http://www.rcsb.org./pdb) was used as a model compound for CT-DNA [4.31]. X-ray crystal structures of the complexes were used as received from X-ray single crystal data. Used spherical polar Fourier correlations were used to perform docking. The following parameters are used for docking: correlation type - shape only, FFT mode - 3D, grid dimension - 0.6, receptor range - 180, ligand range - 180, twist range - 360, distance range - 40. PyMol software was used for visualization of the docked pose.

Serum albumin-complex docking

The AutoDock4.2 [4.32] software was used to perform SAs-complex docking study. For docking study crystal structures of BSA (PDB ID: 4f5s) and HSA (PDB ID: 1ao6), has been downloaded from protein data bank (http://www.rcsb.org/pdb), and the Chimera program (http://www.cgl.ucsf.edu/chimera/) was used for receptor preparation. During docking calculation, the SAs were kept rigid and complexes being docked were kept flexible. The docking results were visualized by Chimera (http://www.cgl.ucsf.edu/chimera/) and PyMol software.

4.3 Results and discussion

4.3.1 Synthetic aspect

The Schiff base ligand, H_2L, was prepared by a one pot synthesis employing condensation of 2-amino-1-butanol and 2-hydroxy-3-ethoxybenzaldehyde in methanol solution under reflux condition, using H_2L, complexes **1** and **2** were synthesized at room temperature.

4.3.2 Crystal structures

The molecular structures of **1** and **2** are presented in Fig. 4.1 and Fig. 4.2, and selected inter atomic distances and angles are provided in Table 4.2 and Table 4.3. Complex **1** crystallizes in the orthorhombic crystal system with Pbca space group, whereas complex **2** crystallizes in the monoclinic crystal system with P21/c space group.

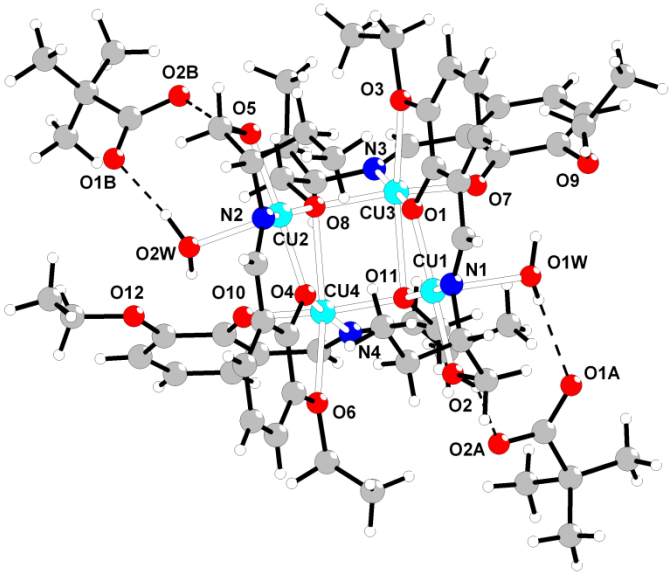

Fig. 4.1 Molecular structure of **1** with labeling of selected atoms. The structure displays some disorder, some atoms were refined over two positions, and other ones were refined using constraints.

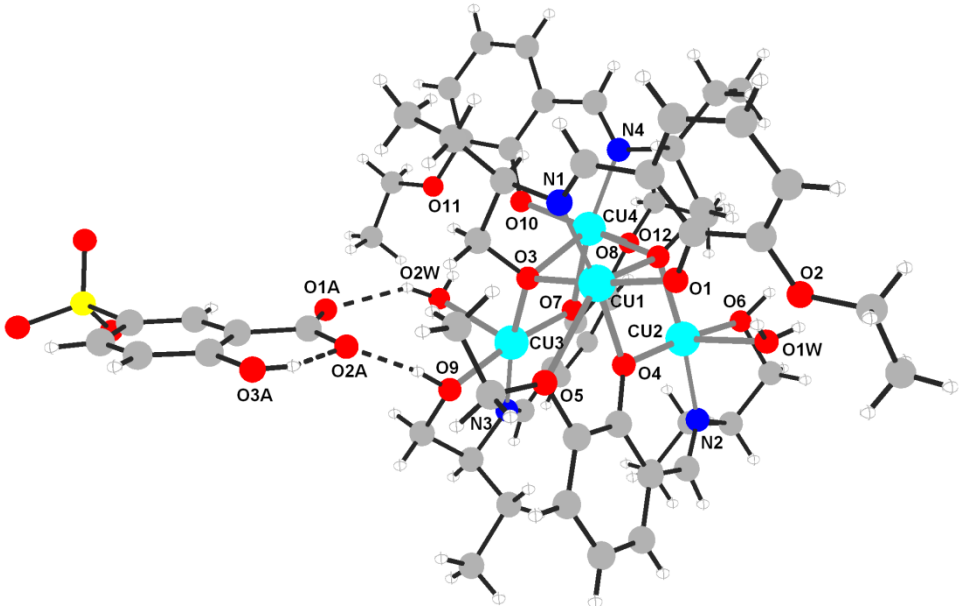

Fig. 4.2 Molecular structure **2** with labeling of selected atoms.

Both the complexes are tetranuclear and posses double open cubane core like structure cationic units with different counter anionic part (two pivalate molecules in complex **1**, whereas one sulfosalicylate molecule in **2**). The cationic unit of both the complexes consist of four copper(II) centers, two water molecules, two monodeprotonated ligands [HL^-], and two dideprotonated ligands [L^{2-}]. Both HL^- behaves as tetradentate ligand and connected with two copper atoms via μ_2-η^1:η^1:η^1:η^2-*O,O,N,O* coordination mode, whereas both L^{2-} behaves as tridentate ligand (ethoxy oxygen atoms remain uncoordinated) and chelates with remaining two copper centre as well as link the earlier moiety with the alkoxo-O atom (μ_3-η^1:η^1:η^3-*O,N,O* coordination mode). Fig. 4.3 and Fig. 4.4 represent the simplified coordination environment around the four Cu(II) centers of complexes **1** and **2**, respectively. Two copper ions [Cu(1) and Cu(2) for **1**; Cu(2) and Cu(3) for **2**] present in distorted square pyramidal geometry (as confirmed by the values of the Addition distortion index [4.33]) while other two metal center [Cu(3) and Cu(4) for **1**; Cu(1) and Cu(4) for **2**] present in distorted octahedral geometry for both the complexes.

Table 4.2 Coordination bond lengths [Å] and bond angles [°] for **1** and **2**.

1		**2**	
Cu(1)-O(1)	1.977(4)	Cu(1)-O(1)	1.911(3)
Cu(1)-O(1W)	2.381(6)	Cu(1)-O(3)	1.959(3)
Cu(1)-O(2)	2.008(6)	Cu(1)-O(4)	2.016(3)
Cu(1)-O(11)	1.921(4)	Cu(1)-O(5)	2.558(3)
Cu(1)-N(1)	1.949(6)	Cu(1)-O(12)	2.493(3)
Cu(2)-O(2W)	2.284(4)	Cu(1)-N(1)	1.936(4)
Cu(2)-O(4)	1.969(4)	Cu(2)-O(1W)	2.341(4)
Cu(2)-O(5)	2.011(4)	Cu(2)-O(4)	1.961(2)
Cu(2)-O(8)	1.923(4)	Cu(2)-O(6)	2.041(3)
Cu(2)-N(2)	1.932(5)	Cu(2)-O(12)	1.914(3)
Cu(3)-O(1)	2.040(4)	Cu(2)-N(2)	1.933(4)
Cu(3)-O(3)	2.472(7)	Cu(3)-O(2W)	2.297(4)
Cu(3)-O(7)	1.899(6)	Cu(3)-O(3)	1.925(3)
Cu(3)-O(8)	1.945(4)	Cu(3)-O(7)	1.968(3)
Cu(3)-O(11)	2.499(4)	Cu(3)-O(9)	2.014(3)
Cu(3)-N(3)	1.956(7)	Cu(3)-N(3)	1.947(4)
Cu(4)-O(4)	2.029(4)	Cu(4)-O(3)	2.475(2)
Cu(4)-O(6)	2.468(5)	Cu(4)-O(7)	2.027(3)
Cu(4)-O(8)	2.477(4)	Cu(4)-O(8)	2.437(4)
Cu(4)-O(10)	1.918(4)	Cu(4)-O(10)	1.896(3)
Cu(4)-O(11)	1.949(4)	Cu(4)-O(12)	1.961(2)
Cu(4)-N(4)	1.929(6)	Cu(4)-N(4)	1.946(4)
Cu(1)-O(1)-Cu(3)	106.5(2)	Cu(1)-O(3)-Cu(3)	121.83(13)
Cu(2)-O(8)-Cu(3)	121.6(2)	Cu(3)-O(3)-Cu(4)	91.47(10)
Cu(2)-O(8)-Cu(4)	91.93(17)	Cu(1)-O (3)-Cu(4)	94.34(10)
Cu(3)-O(8)-Cu(4)	95.01(16)	Cu(1)-O(4)-Cu(2)	105.10(11)
Cu(1)-O(11)-Cu(3)	92.51(17)	Cu(3)-O(7)-Cu(4)	105.26(13)
Cu(1)-O(11)-Cu(4)	121.9(2)	Cu(2)-O(12)-Cu(4)	120.37(15)
Cu(3)-O(11)-Cu(4)	94.22(16)	Cu(1)-O(12)-Cu(4)	93.76(10)

Addison distortion index [4.33] τ_5 for the five coordinated metal centre are 0.042 for Cu(1), 0.175 for Cu(2) in complex **1** whereas 0.082 for Cu(2), 0.041 for Cu(3) in complex **2**, indicating little deviations from ideal square pyramidal geometries. The basal plane of the square pyramid is constructed by the imine nitrogen, the phenolate and the alkoxide oxygen atoms of HL^- and μ_3-alkoxido oxygen atom of a L^{2-}, whereas the apical position is occupied by the O-atom of the coordinated water molecule. The basal coordination bond distances are in between 1.921(4) -

2.011(4) Å for **1** and 1.914(3) - 2.041(3) Å for **2**. On the other hand the apical bond distances are somewhat more distant, being at 2.381(6) and 2.284(4) Å for Cu1 and Cu2, respectively in **1** while 2.341(4) Å for Cu(2) and 2.297(4) Å for Cu(3) in **2** (Table 4.2).

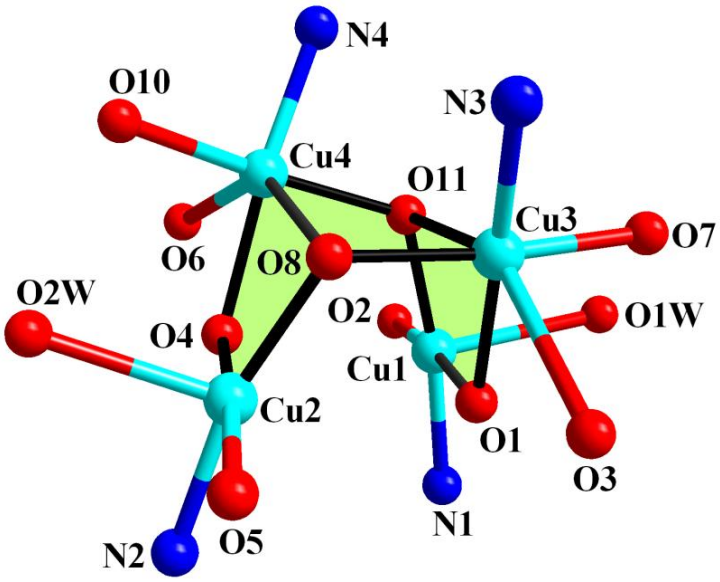

Fig. 4.3 Representation of the tetranuclear copper(II) core in **1** with the coordination environment of the copper(II) centers.

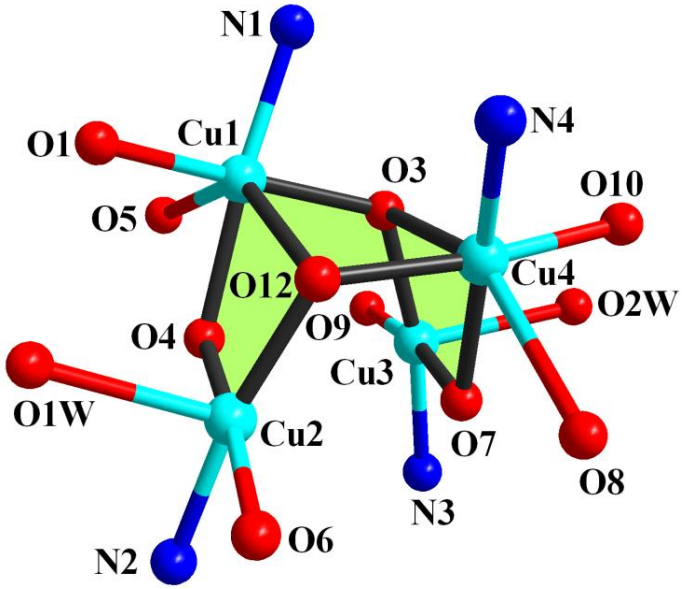

Fig. 4.4 Representation of the tetranuclear copper(II) core in **2** with the coordination environment of the copper(II) centers.

Table 4.3 Coordination bond angles [º] for **1** and **2**

1		**2**	
O(1)-Cu(1)-O(1W)	94.58(19)	O(1)-Cu(1)-O(3)	172.95(10)
O(1)-Cu(1)-O(2)	174.5(2)	O(1)-Cu(1)-O(4)	91.94(11)
O(1)-Cu(1)-O(11)	87.06(18)	O(1)-Cu(1)-O(5)	94.13(10)
O(1)-Cu(1)-N(1)	91.6(2)	O(1)-Cu(1)-O(12)	90.48(10)
O(1W)-Cu(1)-O(2)	87.7(2)	O(1)-Cu(1)-N(1)	94.55(13)
O(1W)-Cu(1)-O(11)	95.63(18)	O(3)-Cu(1)-O(4)	89.89(11)
O(1W)-Cu(1)-N(1)	92.4(2)	O(3)-Cu(1)-O(5)	92.90(10)
O(2)-Cu(1)-O(11)	97.8(2)	O(3)-Cu(1)-O(12)	83.53(9)
O(2)-Cu(1)-N(1)	83.2(2)	O(3)-Cu(1)-N(1)	83.89(13)
O(11)-Cu(1)-N(1)	172.0(2)	O(4)-Cu(1)-O(5)	70.03(9)
O(2W)-Cu(2)-O(4)	87.93(16)	O(4)-Cu(1)-O(12)	73.14(9)
O(2W)-Cu(2)-O(5)	91.05(16)	O(4)-Cu(1)-N(1)	173.25(12)
O(2W)-Cu(2)-O(8)	103.34(18)	O(5)-Cu(1)-O(12)	143.01(10)
O(2W)-Cu(2)-N(2)	91.3(2)	O(5)-Cu(1)-N(1)	107.59(12)
O(4)-Cu(2)-O(5)	175.81(18)	O(12)-Cu(1)-N(1)	108.59(12)
O(4)-Cu(2)-O(8)	86.53(17)	O(1W)-Cu(2)-O(4)	90.05(11)
O(4)-Cu(2)-N(2)	92.7(2)	O(1W)-Cu(2)-O(6)	89.50(13)
O(5)-Cu(2)-O(8)	97.65(18)	O(1W)-Cu(2)-O(12)	97.78(12)
O(5)-Cu(2)-N(2)	83.3(2)	O(1W)-Cu(2)-N(2)	91.91(14)
O(8)-Cu(2)-N(2)	165.3(2)	O(4)-Cu(2)-O(6)	175.20(12)
O(1)-Cu(3)-O(3)	71.2(2)	O(4)-Cu(2)-O(12)	88.91(10)
O(1)-Cu(3)-O(7)	90.5(2)	O(4)-Cu(2)-N(2)	92.16(13)
O(1)-Cu(3)-O(8)	92.96(17)	O(6)-Cu(2)-O(12)	95.89(12)
O(1)-Cu(3)-O(11)	71.72(16)	O(6)-Cu(2)-N(2)	83.07(14)
O(1)-Cu(3)-N(3)	173.3(2)	O(12)-Cu(2)-N(2)	170.26(14)
O(3)-Cu(3)-O(7)	88.7(3)	O(2W)-Cu(3)-O(3)	98.45(12)
O(3)-Cu(3)-O(8)	98.4(2)	O(2W)-Cu(3)-O(7)	94.72(12)
O(3)-Cu(3)-O(11)	142.92(19)	O(2W)-Cu(3)-O(9)	90.59(12)
O(3)-Cu(3)-N(3)	103.6(3)	O(2W)-Cu(3)-N(3)	91.80(14)
O(7)-Cu(3)-O(8)	172.7(2)	O(3)-Cu(3)-O(7)	87.67(11)
O(7)-Cu(3)-O(11)	91.7(2)	O(3)-Cu(3)-O(9)	97.23(12)
O(7)-Cu(3)-N(3)	93.6(2)	O(3)-Cu(3)-N(3)	169.75(13)
O(8)-Cu(3)-O(11)	83.35(16)	O(7)-Cu(3)-O(9)	172.20(12)
O(8)-Cu(3)-N(3)	83.6(2)	O(7)-Cu(3)-N(3)	91.72(14)
O(11)-Cu(3)-N(3)	113.4(3)	O(9)-Cu(3)-N(3)	82.38(15)
O(4)-Cu(4)-O(6)	70.41(17)	O(3)-Cu(4)-O(7)	72.80(10)
O(4)-Cu(4)-O(8)	71.84(15)	O(3)-Cu(4)-O(8)	144.12(11)
O(4)-Cu(4)-O(10)	93.99(18)	O(3)-Cu(4)-O(10)	89.54(10)
O(4)-Cu(4)-O(11)	89.39(17)	O(3)-Cu(4)-O(12)	83.98(9)
O(4)-Cu(4)-N(4)	171.3(2)	O(3)-Cu(4)-N(4)	114.81(12)
O(6)-Cu(4)-O(8)	142.25(16)	O(7)-Cu(4)-O(8)	71.33(11)
O(6)-Cu(4)-O(10)	91.63(19)	O(7)-Cu(4)-O(10)	92.23(12)
O(6)-Cu(4)-O(11)	95.84(18)	O(7)-Cu(4)-O(12)	90.28(11)
O(6)-Cu(4)-N(4)	105.3(3)	O(7)-Cu(4)-N(4)	170.12(13)
O(8)-Cu(4)-O(10)	90.81(16)	O(8)-Cu(4)-O(10)	91.03(12)
O(8)-Cu(4)-O(11)	83.85(16)	O(8)-Cu(4)-O(12)	96.94(12)
O(8)-Cu(4)-N(4)	112.1(3)	O(8)-Cu(4)-N(4)	100.93(13)
O(10)-Cu(4)-O(11)	172.47(19)	O(10)-Cu(4)-O(12)	172.04(12)
O(10)-Cu(4)-N(4)	93.7(2)	O(10)-Cu(4)-N(4)	94.07(14)
O(11)-Cu(4)-N(4)	83.5(2)	O(12)-Cu(4)-N(4)	84.50(13)

In **1** the angles between the successive coordinating equatorial atoms with Cu(1) are 83.19(2)°, 87.06(18)°, 91.63(2)° and 97.80(2)° and the angles between the axial atom, Cu(1) and equatorial atoms are 87.66(2)°, 92.38(2)°, 94.58(19)° and 95.63(18)° whereas in Cu(2) the angles between the successive coordinating equatorial atoms with Cu(2) are 83.31(2)°, 86.53(17)°, 92.65(2)° and 97.65(18)° and the angles between the axial atom, Cu(2) and equatorial atoms are 87.93(16)°, 91.05(16)°, 91.29(2)° and 103.34(18)°. In **2** the angles between the successive coordinating equatorial atoms with Cu(2) are 83.07(14)°, 88.91(10)°, 92.16(13)° and 95.89(12)° and the angles between the axial atom, Cu(2) and equatorial atoms are 89.50(13)°, 90.05(11)°, 91.91(14)° and 97.78(12)° whereas in Cu(3) the angles between the successive coordinating equatorial atoms with Cu(3) are 82.38(15)°, 87.67(11)°, 91.72(14)° and 97.23(12)°, and the angles between the axial atom, Cu(3) and equatorial atoms are 90.59(12)°, 91.80(14)°, 94.72(12)° and 98.45(12)°. Other two metal centers in the coordination sphere i.e., Cu(3) and Cu(4) for complex **1**; Cu(1) and Cu(4) for complex **2** are remains in distorted octahedral geometry. The phenoxido oxygen, imine nitrogen and alkoxido oxygen of one L^{2-} and μ_2-phenoxido oxygen of HL^- formed the basal plane of the octahedron, whereas ethoxy oxygen of same HL^- and the alkoxido oxygen of another L^{2-} occupied the axial positions. The equatorial bond lengths are in the range 1.899(6) - 2.040(4) Å for **1** and 1.896(3) - 2.027(3) Å for **2**, whereas the axial bond lengths are somewhat more than the equatorial bond lengths due to the Jahn-Teller distortion and ranges between 2.468(5) to 2.499(4) Å for **1** and 2.437(4) to 2.558(3) Å for **2**. The Cu(1)-O(4) and Cu(2)-O(1) distances for **1** and Cu(2)-O(7) and Cu(3)-O(4) for **2** are long of 2.991, 3.106, 2.968 and 3.004 Å respectively. These long distances between copper and oxygen atoms are the responsible for the formation of double open cubane core structure. The trans angles are in between 70.41(17)° to 113.39(3)° and the cis angles ranges between 83.49(2)°

to 93.99(18)° for **1**, whereas for **2** these are between 70.03(9)° to 114.81(12)° and 83.89(13)° to 94.55(13)°. The four copper atoms are placed at the vertices of a distorted tetrahedron with edge length ranges between 3.187 to 4.006 Å for **1** and 3.157 to 3.860 Å for **2**, the Cu(1)-Cu(2) distance for **1** and Cu(2)-Cu(3) distance for **2** of 4.006 Å and 3.860 Å respectively are the longest (Figs. 4.5 and 4.6).

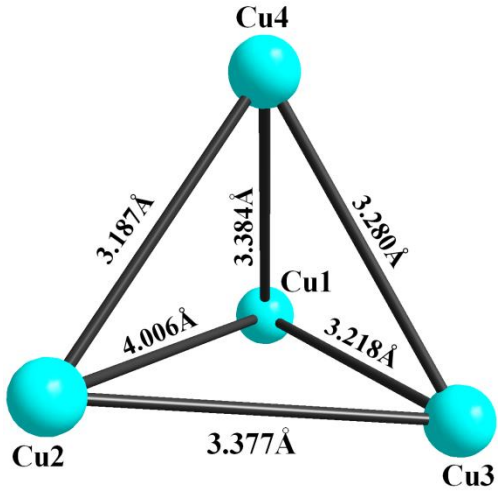

Fig. 4.5 Arrangement of four copper atoms in complex **1**.

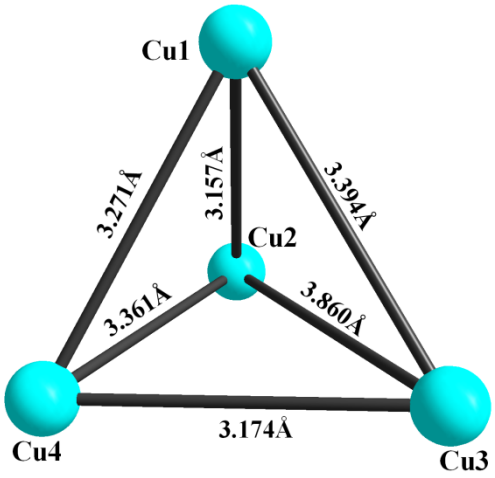

Fig. 4.6 Arrangement of four copper atoms in complex **2**.

Alvarez et al. categorize [4.34] the copper cubane into three types according to the Cu…Cu distances within the Cu_4O_4 cubane core: (i) (2+4), with two short and four long Cu…Cu

distances; (ii) (4+2), with two long and four short Cu…Cu distances; and (iii) (6+0), with six similar Cu…Cu distances [4.34c]. In the core structure of both the complexes six Cu…Cu distances show a 3:2:1 and not 4:2 or 2:4 analogy, and hence Cu_4O_4 core of both the complexes cannot be classified as above three systems.

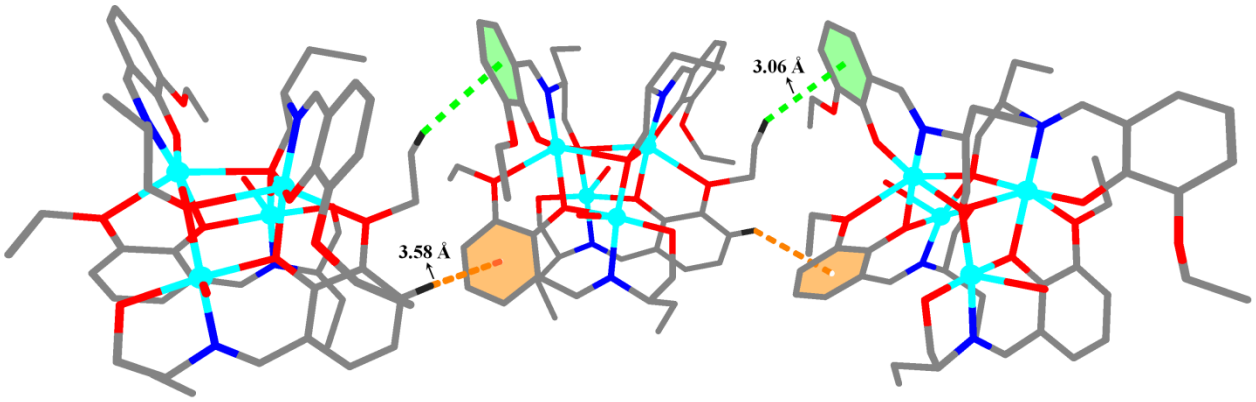

Fig. 4.7 1D supramolecular architecture of **1** formed by C-H…π interactions.

Complex **1** formed 1D supramolecular structure (Fig. 4.7) through two different C-H...π interactions [4.35] (C-H...Cg = 3.066 Å, 3.586 Å). Alternatively, packing diagram of **2** shows that it is also exist as a 1D layer (Fig. 4.8) formed with two different C-H...π interactions (C-H...Cg = 2.922 Å and 3.306 Å).

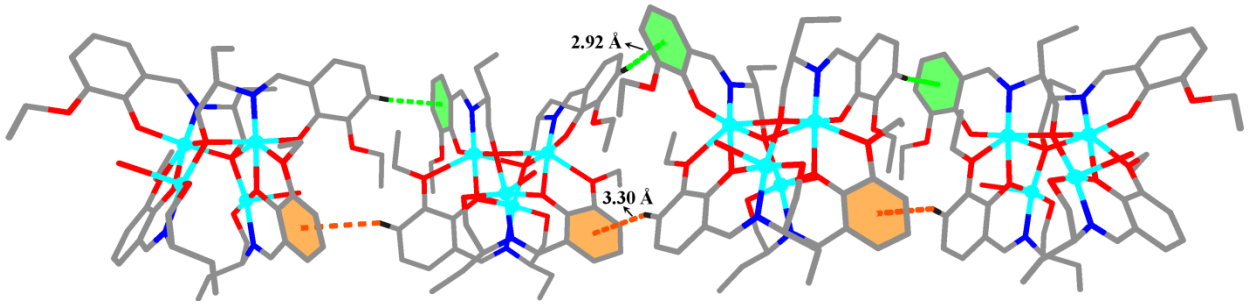

Fig. 4.8 1D supramolecular architecture of **2** formed by C-H…π interactions.

Table 4.4 C-H…π interactions in complex **1**

X-H(I)...Cg(J)	H..Cg	X-H..Cg	X..Cg
C(10)-H(10B)…Cg(18)	2.72	153	3.611(10)
C(23)-H(23B)…Cg(17)	2.88	141	3.685(10)
C(13)-H(13C)…Cg(20)	3.06	139	3.84
C(3)-H(3)… Cg(18)	3.58	133	4.27
Cg(17) = C(1)-C(2)-C(3)-C(4)-C(5)-C(6)			
Cg(18) = C(14)-C(15)-C(16)-C(17)-C(18)-C(19)			
Cg(20) = C(40)-C(41)-C(42)-C(43)-C(44)-C(45)			

Table 4.5 C-H…π interactions in complex **2**

X-H(I)...Cg(J)	H..Cg	X-H..Cg	X..Cg
C(25)-H(25A)…Cg(18)	2.78	148	3.636(7)
C(38)-H(38A)…Cg(17)	2.55	156	3.457(8)
C(42)-H(42)…Cg(16)	2.92	175	3.849(5)
C(16)-H(16)…Cg(18)	3.30	159	4.18
Cg(16) = C(1)-C(2)-C(3)-C(4)-C(5)-C(6)			
Cg (17) = C(14)-C(15)-C(16)-C(17)-C(18)-C(19)			
Cg (18) = C(27)-C(28)-C(29)-C(30)-C(31)-C(32)			

.

4.3.3 IR, electronic absorption and fluorescence spectra of complexes

The most important absorption bands in IR spectra of complex **1** and **2** (Figure 4.9 and 4.10) are summarized in experimental section and tabulated in Table 4.6.

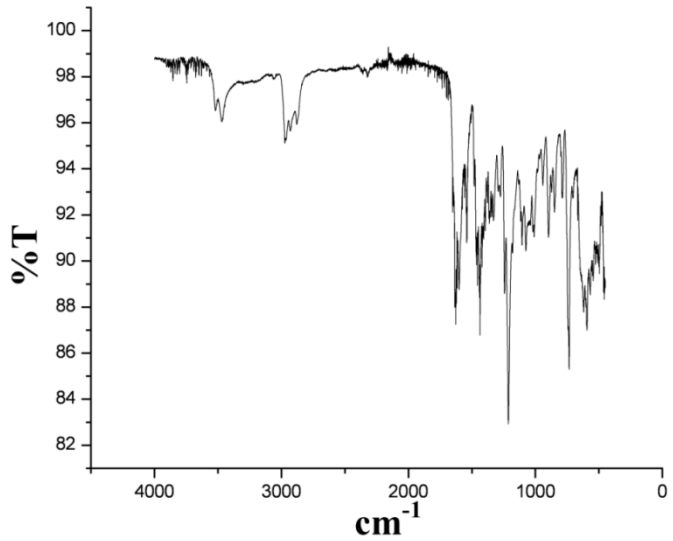

Fig. 4.9 IR spectrum of complex **1**

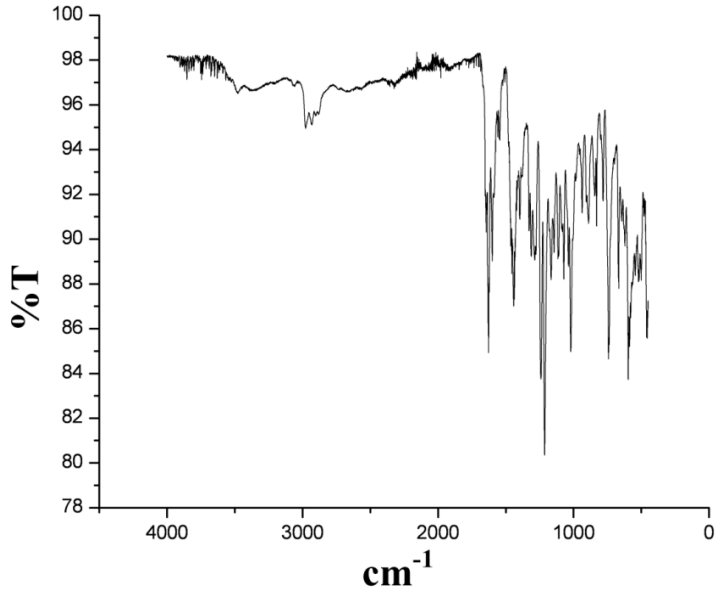

Fig. 4.10 IR spectrum of complex **2**

Table 4.6 Electronic absorption and emission spectra of complexes

	UV-vis [a]λ_{max}; [b]ε ($M^{-1}cm^{-1}$)	Emission (nm)	$\Delta\nu$[c], (nm)	Φ_s	[d]FT-IR, [e](cm^{-1})
1	221 (1.22×10^5), **267** (6.44×10^4), 346 (1.68×10^4)	329, 516, 620	62, 249, 353	0.41	3470(br) [ν(O-H)]; 2970 [ν(C-H)]; 1627, 1436(vs) [ν(-COOH)]; 1541 [ν(C=N)]
2	205 (6.18×10^4), 231 (5.42×10^4), **277** (2.92×10^4), 379 (8.20×10^3)	315, 413	38, 136	0.46	3481(br) [ν(O-H)]; 2980 [ν(C-H)]; 1627, 1441(vs) [ν(-COOH)]; 1544 [ν(C=N)]

Bold number indicates the excitation wavelengths. [a]Wavelength in nanometer, [b]Molar extinction coefficient in M^{-1} cm^{-1} in methanol solvent. [c]Stoke shift. [d]In KBr pellet, [e]wave number in cm^{-1}.

Both the complexes exhibits a strong broad band in the region 3400 - 3600 cm^{-1} is due to the ν(O-H) stretching vibration [4.36]. The bands at 2970 (for **1**) and 2980 (for **2**) cm^{-1} corresponds to the aromatic ν(C-H) stretching vibrations and aliphatic ν(C-H) stretching vibrations for both the complexes appears in the region 2930 cm^{-1} to 2875 cm^{-1}. The asymmetric and symmetric stretching vibrations of the carboxylate group for complex **1** appear at 1627 cm^{-1} and 1436 cm^{-1}, whereas for **2** these are 1627 cm^{-1} and 1441 cm^{-1}, respectively. The strong and sharp bands at 1541 cm^{-1} for **1** and 1544 cm^{-1} for **2** is due to the aliphatic (C=N) stretching vibration. For **2** the bands at 1397 cm^{-1} and 1287 cm^{-1} corresponds to $\nu_{as}(SO_2)$ and $\nu_s(SO_2)$, respectively. On the other

hand band at 1243 (for **1**) and 1241 (for **2**) cm^{-1} corresponding to ν(O-Et) stretching vibrations. Stretching vibrations of coordinated water for complex **1** appears at 897 cm^{-1} (ρ_r) and 621 cm^{-1} (ρ_w), whereas for complex **2** these bands are appears at 889 cm^{-1} (ρ_r) and 667 cm^{-1} (ρ_w).

The electronic absorption spectrum of the complexes shows in Fig. 4.11. Complex **1** shows significant transitions at 221 nm ($\varepsilon \sim 1.22 \times 10^5$ liter $mole^{-1}$ cm^{-1}), 267 nm ($\varepsilon \sim 6.44 \times 10^4$ liter $mole^{-1}$ cm^{-1}) and 346 nm ($\varepsilon \sim 1.68 \times 10^4$ liter $mole^{-1}$ cm^{-1}), whereas complex **2** shows significant transitions at 205 nm ($\varepsilon \sim 6.18 \times 10^4$ liter $mole^{-1}$ cm^{-1}), 231 nm ($\varepsilon \sim 5.42 \times 10^4$ liter $mole^{-1}$ cm^{-1}), 277 nm ($\varepsilon \sim 2.92 \times 10^4$ liter $mole^{-1}$ cm^{-1}) and 379 nm ($\varepsilon \sim 8.20 \times 10^3$ liter $mole^{-1}$ cm^{-1}). Result of the study of luminescence properties are summarized in Table 4.6. Both the complexes exhibit red shifted emission. On excitation at 267 nm complex **1** exhibits luminescence bands at 329, 516 and 620 nm (Fig. 4.12) with a fluorescence quantum yield Φ_s= 0.41, whereas complex **2** upon excitation at 277 nm exhibits emission band at 315 and 413 nm with fluorescence quantum yield Φ_s = 0.46. The positions of emission bands remain unchanged when λ_{ex} is varied between (λ_{ex} - 10) and (λ_{ex} + 10) nm.

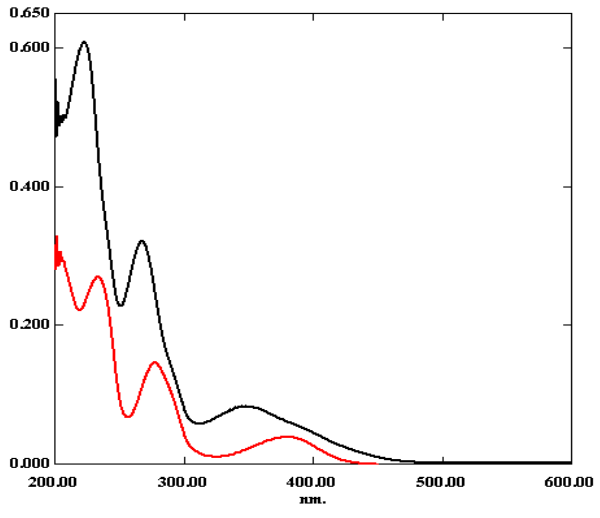

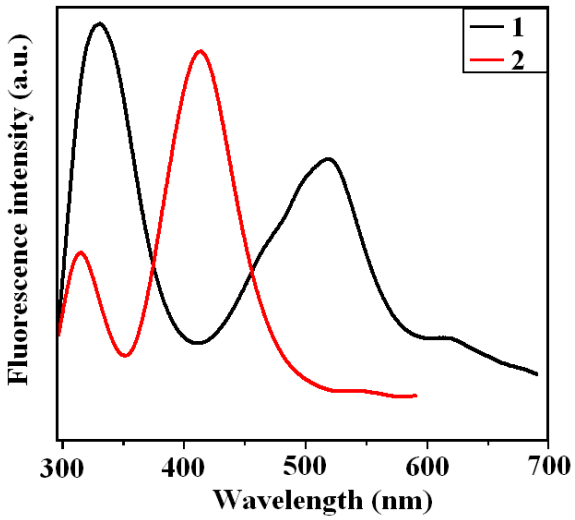

4.3.4 Protein Binding Studies

To understand the mechanism of interaction between complexes and serum albumins, absorption titration experiments and fluorescence quenching experiments has been performed.

Absorption spectral studies

The change in the UV-vis absorption spectra upon incremental addition (10 µL, 0.3475 mmol) of complex solutions (at 300 K) to the solution of BSA (3 ml, 0.492 µM) and HSA (3 ml, 0.334 µM) are shown in Figs. 4.13 and 4.14, respectively. Enhancement of the absorption intensities were observed for both the spectrum of BSA and HSA along with small hypsochromic shift (3 nm for **1**; 2 nm for **2**). Hypsochromic shift of absorption spectral band indicate the presence of a static interaction between serum albumins and the Cu(II) complexes [4.37]. From the plot of 1/[complex] vs $1/(A_{abs}-A_0)$ (Fig. 4.15) of the following equation the apparent association constant (K_a) were evaluated.

$$\frac{1}{(A_{obs} - A_0)} = \frac{1}{(A_c - A_0)} + \frac{1}{K_a(A_c - A_0)[complex]}$$

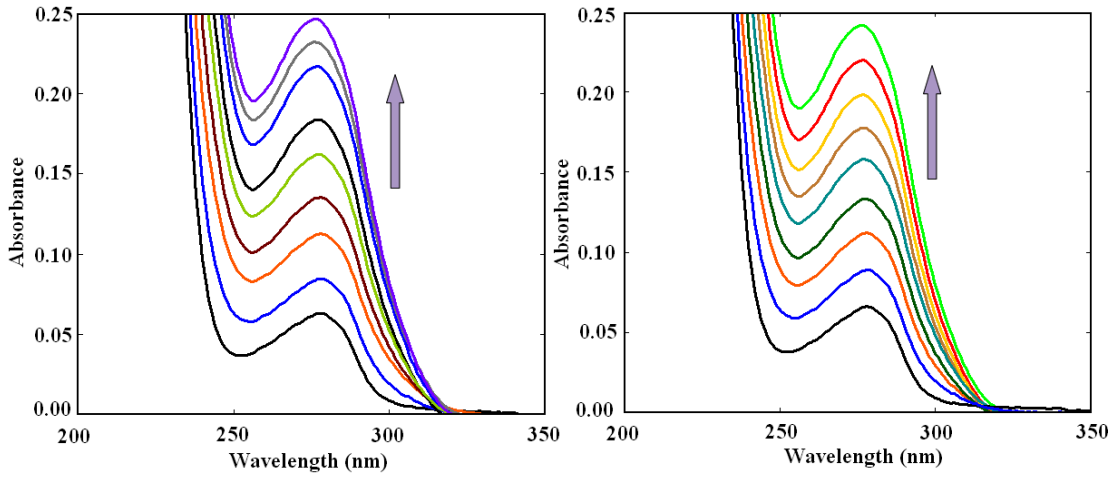

Fig. 4.13 UV-Vis absorption spectra of **1**-BSA (left) and **2**-BSA (right) upon gradual addition of 10 µl 0.3475 µM aqueous solutions of complexes at room temperature.

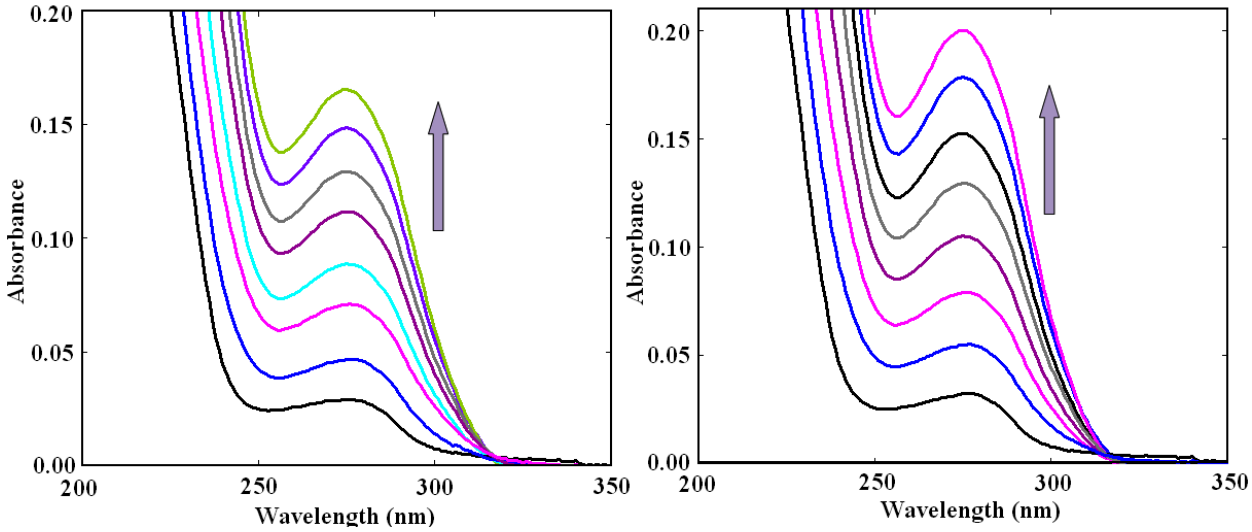

Fig. 4.14 UV-Vis absorption spectra of **1**-HSA (left) and **2**-HSA (right) upon gradual addition of 10 µl 0.3475 µM aqueous solutions of complexes at room temperature.

The values of apparent association constant (K_a) are 1.64×10^4, 2.48×10^4, 5.79×10^3 and 5.98×10^3 M^{-1} for **1**-BSA, **2**-BSA, **1**-HSA and **2**-HSA, respectively (Table 4.7). The order of association constant values are comparable to those reported for copper(II)-Schiff base complexes [4.38].

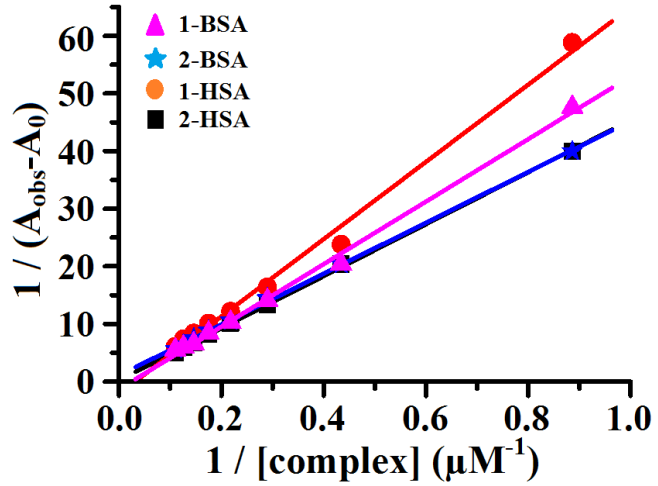

Fig. 4.15 Plot of 1/[complex] vs 1/ (A_{obs}-A_0) for the calculation of apparent association constant (K_{app}).

Table 4.7 Quenching Constant (K_q), Binding Constant (K_{bin}), number of Binding Sites (n) and the values of apparent association constant (K_a) for the Interactions of Complexes with BSA and HSA

	Complexes	K_{sv} (M^{-1})	K_q ($M^{-1}S^{-1}$)	K_{bin} (M^{-1})	n	K_a (M^{-1})
BSA	**1**	1.15×10^5	2.30×10^{13}	9.58×10^4	1.07	1.64×10^4
	2	1.92×10^5	3.84×10^{13}	2.29×10^5	0.99	2.48×10^4
HSA	**1**	1.18×10^5	2.36×10^{13}	8.76×10^4	1.11	5.79×10^3
	2	1.32×10^5	2.64×10^{13}	2.67×10^5	0.96	5.98×10^3

Fluorescence spectroscopic studies

Fluorescence titration experiments have been carried out using fixed concentration of SA (0.492 µM BSA and 0.334 µM HSA) at room temperature and varying the concentration of complexes (0 - 9.02 µM) in the range 290 - 450 nm (λ_{ex} = 280 nm, Fig. 4.16).

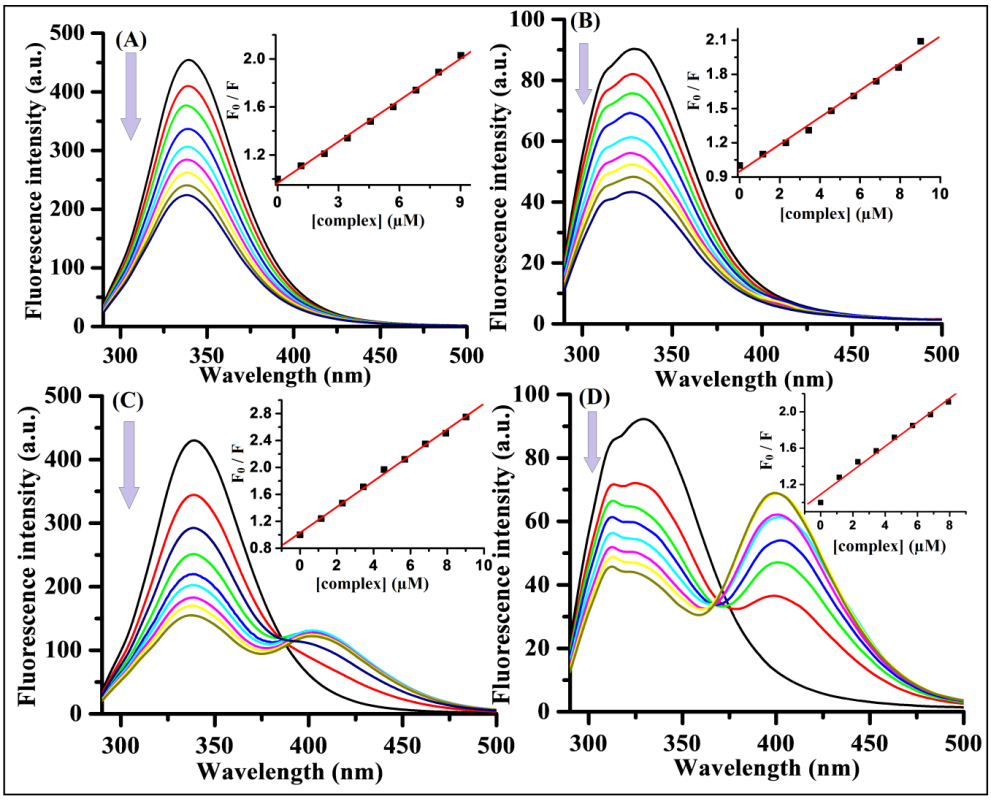

Fig. 4.16 Emission spectrum of BSA (λ_{ex} = 280 nm; λ_{em} = 340 nm) and HSA in the presence of increasing amounts of complexes. Arrow shows that the emission intensity changes upon increasing complex concentration.

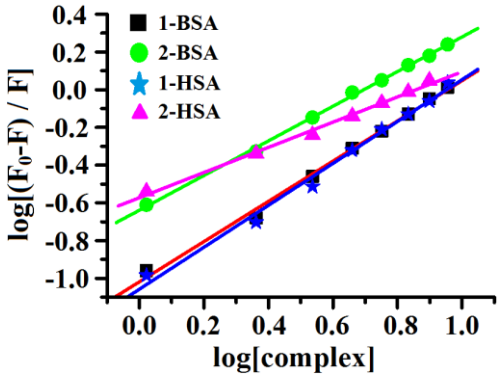

Fig. 4.17 Scatchard plot of the SA fluorescence titration for complexes.

The fluorescence intensity of BSA at ~340 nm quenched with a small blue shift (50.76%, 3 nm, **1**; 63.34%, 3 nm, **2**), whereas for HSA at ~330 nm these are (52.16%, 3 nm, **1**; 52.79%, 2 nm, **2**). The blue shift primarily occurs due to the presence of the active site of the protein in a hydrophobic environment. From the fluorescence experiment it is clear that some interaction is taking place between the complexes and SA. Fluorescence quenching data were analyzed with the Stern-Volmer equation [4.23]:

$$F_0/F = 1 + K_{sv}[complex] = 1 + k_q\tau_0[complex]$$

where F_0 and F are the fluorescence intensities in the absence and in the presence of the complex, and τ_0 is the lifetime of serum albumin (~ 5×10^{-9} s) [4.28].

To have a deep insight into the quenching sequence, the equilibrium binding constant (K_{bin}) and number of binding site (n) were also evaluated from the plot of log $[(F_o - F)/F]$ versus log [complex] (Fig. 17) using the Scatchard equation [4.29]:

$$\log [(F_o - F)/F] = \log K_{bin} + n \log[complex]$$

The value of Stern-Volmer constant (K_{sv}), quenching costant (K_q) and binding constant (K_{bin}) are 1.15×10^5 M^{-1}, 2.30×10^{13} $M^{-1}S^{-1}$, 9.58×10^4 M^{-1} for **1**-BSA, 1.92×10^5 M^{-1}, 3.84×10^{13} $M^{-1}S^{-1}$, 2.29×10^5 M^{-1} for **2**-BSA, 1.18×10^5 M^{-1}, 2.36×10^{13} $M^{-1}S^{-1}$, 8.76×10^4 M^{-1} for **1**-HSA and 1.32×10^5 M^{-1}, 2.64×10^{13} $M^{-1}S^{-1}$, 2.67×10^5 M^{-1} for **2**-HSA, respectively (Table 4.7). The calculated value of n with serum albumins is around 1 for both the complexes, indicating the existence of just a single binding site in SA for the complexes.

4.3.5 Interaction with Calf-Thymus DNA

Interactions of metal complexes with DNA may be covalent or non-covalent and the possible binding modes are intercalative, groove and electrostatic in non-covalent interactions [4.39]. To investigate the nature of binding of complexes with CT-DNA electronic absorption and emission spectroscopic studies were performed.

Absorbance spectral studies

Electronic absorption spectral studies have been carried out by monitoring the change in absorption intensities of Cu(II) complexes (5 μM) by incremental addition of CT-DNA solution (0-30 μM). Fig. 4.18 shows the absorption spectra of **1** and **2** in the absence and presence of CT-DNA. All the absorption bands of **1** and **2** showed hypochromism after incremental addition of CT-DNA solution. The bands at 221 and 267 nm of **1** showed hypochromism with 4 and 2 nm red shift, while the band at 231 nm of **2** showed hypochromism with 2 nm red shift. On the other hand the band at 346 nm for **1**, and the bands at 277 nm and 379 nm for **2** showed hypochromism without any shift. From the ratio of the slope and the intercept of the [DNA] / (ε_a-ε_f) versus [DNA] plot (inset of Fig. 4.18), intrinsic binding constant (K_{ib}) were evaluated. The magnitude of intrinsic binding constant (K_{ib}) are 2.71×10^4 and 1.58×10^4 M^{-1} for complex **1** and complex **2**, respectively (Table 4.8).

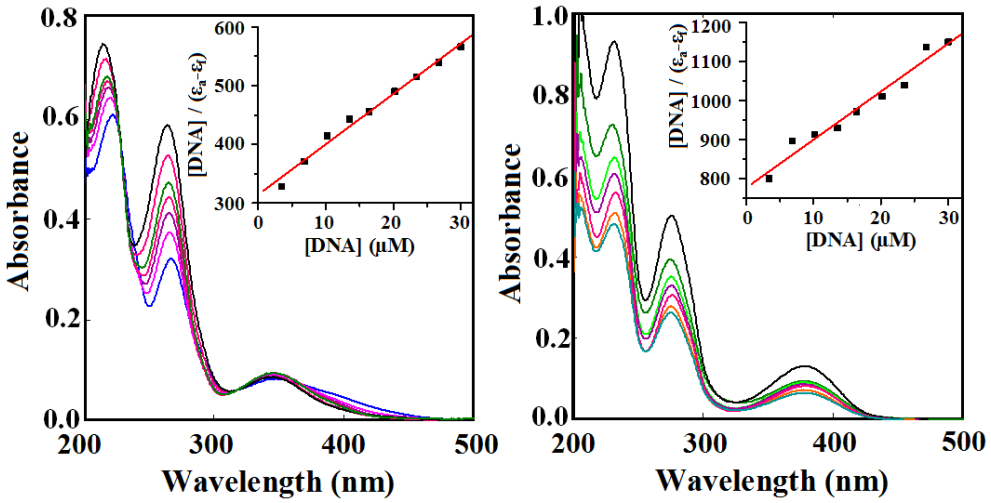

Fig. 4.18 Absorption titration spectra of complexes **1** and **2** in the absence (black line) and presence (other lines) of CT-DNA to complex at room temperature. Inset: Plot of [DNA]/(ε_a-ε_f) versus [DNA]. Arrow shows the absorbance changes upon increasing CT-DNA concentration.

Table 4.8 Electronic spectral properties of the Cu(II) complexes bound to CT-DNA

	λ_{max} (nm)	change in emission	Δε (%)	K_{sv} (M^{-1})	K_{ib} (M^{-1})	K_{app} (M^{-1})
1	602	hypochromism	69.53	2.87×10^5	2.71×10^4	1.75×10^7
2	602	hypochromism	55.84	1.53×10^5	1.58×10^4	1.17×10^7

Competitive binding between Ethidium Bromide and Compounds

Electronic absorption spectral studies indicated that both the Cu(II) complexes bind with CT-DNA. Ethidium bromide exhibit strong fluorescence when excited at 500 nm due to its intercalative binding with CT-DNA [4.40]. The luminescence spectra of CT-DNA bound EB in absence and in presence of complexes were given in Fig. 4.19. On addition Cu(II) complexes (0 - 9.02 μM) to EB (8 μM) bounded CT-DNA (8 μM) results the quenching of emission and the luminescence band showed hypochromism up to 69.53% and 55.84% of the initial emission intensity for complexes **1** and **2**, respectively. Decrease in the fluorescence intensity confirmed that the ethidium bromide molecules are displaced from the CT-DNA binding sites by complex

molecules. The Stern-Volmer plots (insets of Fig. 4.19) are in good agreement (R= 0.9914, 0.9987) with the linear Stern-Volmer equation and confirm that the fluorescence quenching is due to the result of the replacement of EB from EB-DNA by each of the complexes [4.41].

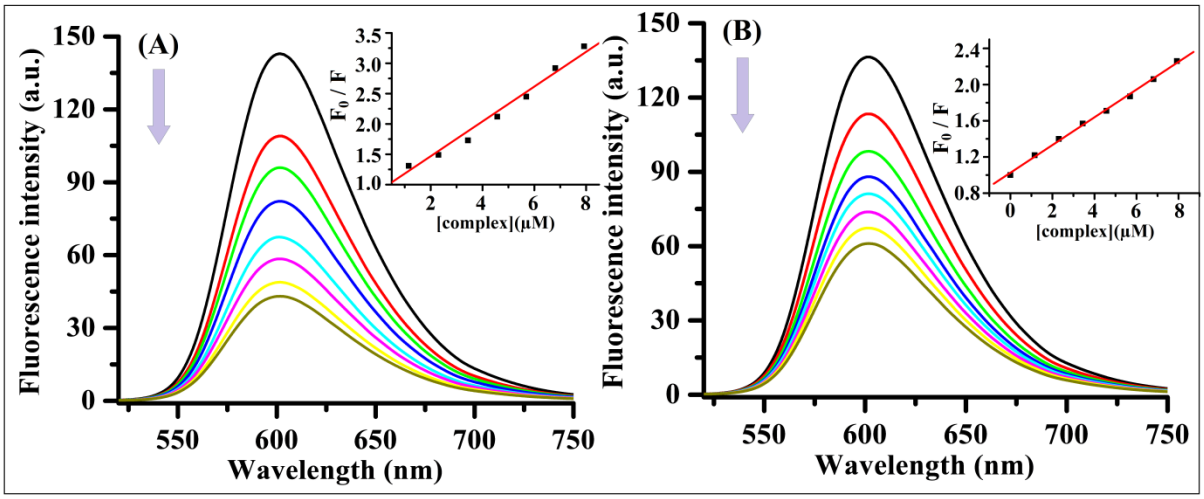

Fig. 4.19 Emission spectra of EB bounded CT-DNA in the presence of complex **1** (A) and complex **2** (B). Inset: Stern-Volmer plot of fluorescence titrations.

The K_{SV} values are 2.87×10^5 and 1.53×10^5 M^{-1} for **1** and **2**, respectively. The apparent binding constant (K_{app}) was evaluated by the following equation [4.37a],

$$K_{EB}[EB] = K_{app}[complex]$$

where [complex] is concentration of complex at the 50% decrease in the emission intensity of ethidium bromide, $K_{EB} = 1.0 \times 10^7$ M^{-1} (DNA binding constant of ethidum bromide), [EB] is the concentration of ethidium bromide (8 μM). The K_{app} values are 1.75×10^7 and 1.17×10^7 M^{-1} for **1** and **2**, respectively (Table 4.8). Table 4.9 shows a comparison of the binding parameters of DNA interaction of the present complexes with reported tetranuclear copper(II) cubane core complexes. The binding parameter values of **1** and **2** are comparable with those reported compounds.

Table 4.9 Kinetic parameters of the interaction of Cu(II) cubane compounds with CT-DNA.

Compound	K_{ib}	K_{sv}	Ref.
$[Cu_4(L)_2(HL)_2(H_2O)_2]\cdot 2(pv)$	2.71×10^4	2.87×10^5	This work
$[Cu_4(L)_2(HL)_2(H_2O)_2]\cdot(ssal)$	1.58×10^4	1.53×10^5	This work
$[Cu_4(L)_2(HL)_2(H_2O)_2]\cdot 2(ClO_4)\cdot DMF$	1.25×10^4	1.483×10^5	[4.9c]
$[Cu_4(L)_2(HL)_2(H_2O)_2]\cdot(tp)$	8.77×10^3	9.78×10^4	[4.9c]
$Cu_4(L^1)_4$	4.50×10^3	-	[4.3g]
$[Cu_4(\mu\text{-}L^2)_2(\mu_{1,1,3,3}\text{-}O_2CH)](OH)\cdot 6H_2O$	3.37×10^4	4.73×10^4	[4.3h]
$[Cu_4((HL^3)_2(H_2L^3)_2(H_2O)(C_2H_5OH)]\cdot 2(ClO_4)\cdot 2(C_2H_5OH)$	1.35×10^4	1.69	[4.3i]
$[Cu_4(H_2L^4)_4\cdot 2H_2O]\cdot 5H_2O$	1.48×10^4	-	[4.3j]
$[Cu_4(H_2L^4)_4\cdot 4H_2O]$	2.54×10^4	-	[4.3j]

H_2L^1 = Schiff base of 1-amino-2-propanol and salicylaldehyde; tp = terephthalate; H_3L^2 =1,3-bis [3-aza-3-(1-methyl-3-oxobut-1-enyl)prop-3-en-1-yl]-2-(2-hydroxyphenyl)- 1,3-imidazolidine; H_3L^3 = 2-ethyl-2-((2-hydroxy-3-methoxybenzylideneamino)propane-1,3-diol); H_4L^4 = 2-[(2-Hydroxy-3-methoxy-benzylidene)-amino]-2-hydroxymethyl-propane-1,3-diol.

4.3.6 *Molecular docking*

Molecular Docking with DNA

Molecular docking techniques are an important tool to understand the interactions between DNA and drug in rational drug design and as well as in the mechanistic study by placing a drug into the binding site of the DNA [4.42]. Molecular docking have been performed on B-DNA (PDB ID: 1bna) in presence of **1** and **2**. Fig. 4.20 exhibits the energetically most favorable conformations of the docked structures of complexes and revealed that both the complexes intercalates within the A-T region of the DNA.

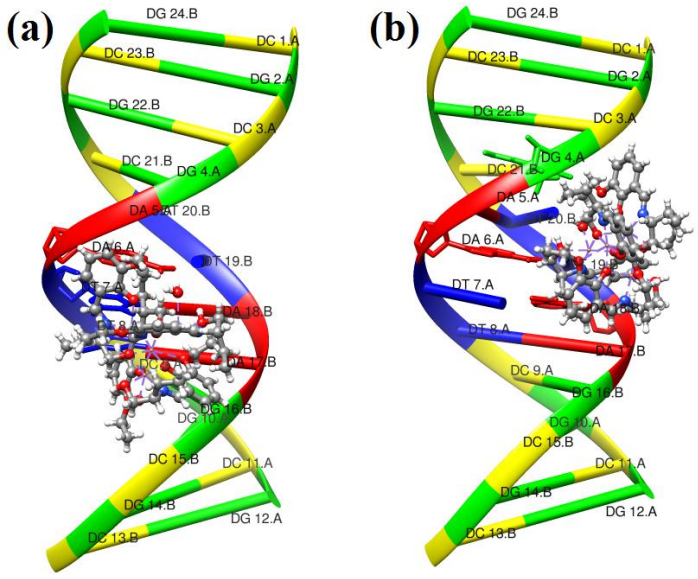

Fig. 4.20 Molecular docked model of complexes **1** (a) and **2** (b) with DNA (PDB ID: 1BNA)

The minimum energy structures indicate that all the complexes are sitting in the major groove of B-DNA with a relative binding energy of -316.4 (**1**) and -316.9 (**2**) Kcal/mole, respectively (Table 4.10). As seen in Table 4.10, there are three categories of hydrophobic contacts between the complex **1** and bases of DNA including, DA 6, DT 7 and DT 8. On the other hand complex **2** also have three hydrophobic contacts with bases of DNA (DG 4, DA 6 and DA 18) and additionally able to form one hydrogen bonding interaction with DA 5. Thus hydrophobic and hydrogen bonding interactions play significant role in stabilizing of the **2**, while hydrophobic interactions stabilizing the complex **1** in the major groove of DNA. The UV-vis spectroscopic study of complexes show hypochromic shifts of absorption spectral bands which indicate that the interaction may occur with intercalation or groove binding. The docking result clearly confirm that the interaction occur through groove binding.

Table 4.10 The results of molecular docking of Cu(II) complexes with DNA

Complexes	Free energy of interaction (Kcal/mole)	Types of interactions	Adjacent nucleotides (within 3 Å distances to complex)
1	-316.4	Hydrophobic	DA 6, DT 7, DT 8
2	-316.9	H-bond and hydrophobic	DA 5, DG 4, DA 6, DA 18

Molecular Docking with BSA

Molecular docking study of the metal compounds with serum albumins help to predict their orientation and binding sites inside the serum albumins. Binding interactions of the complexes with BSA are shown in Figs 4.21-4.24.

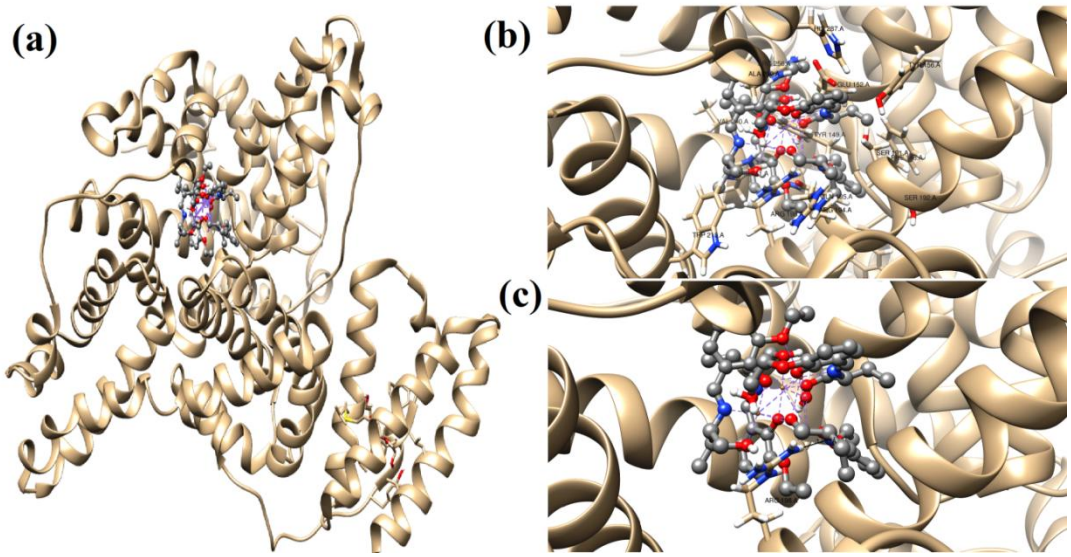

Fig. 4.21 Molecular docking image of complex **1** with BSA (binding site: Tyr149); (a) Interaction of **1** with amino acid residues of BSA (b) Zoom view of interaction of **1** with amino acid residues of BSA (c) H-bonding interaction of **1** with amino acid residues of BSA

Since BSA has two different active sites (*Tyr 149* and *Tyr 410*) for binding, we performed docking of each complex with two binding sites individually in order to investigate effective binding site of BSA for our complexes. Based on chimera score (Table 4.11), it is clear that all the complexes selectively bind with BSA at the site of *Tyr 149*.

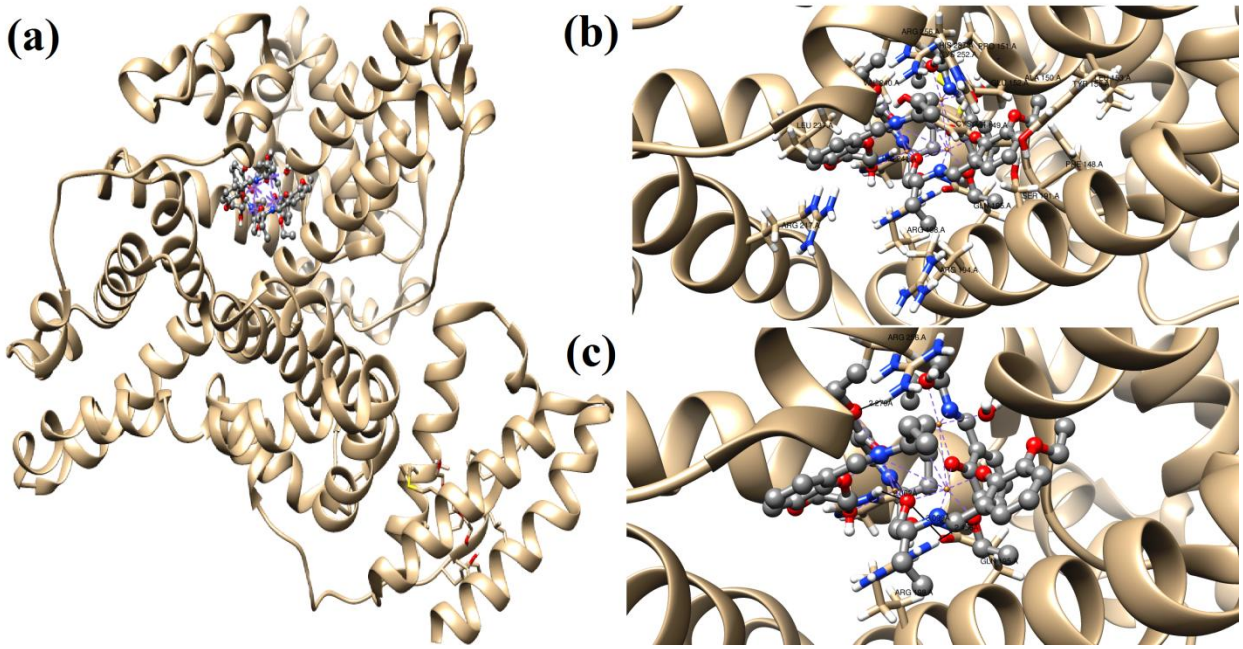

Fig. 4.22 Molecular docking image of complex **2** with BSA (binding site: Tyr149); (a) Interaction of **2** with amino acid residues of BSA (b) Zoom view of interaction of **2** with amino acid residues of BSA (c) H-bonding interaction of **2** with amino acid residues of BSA.

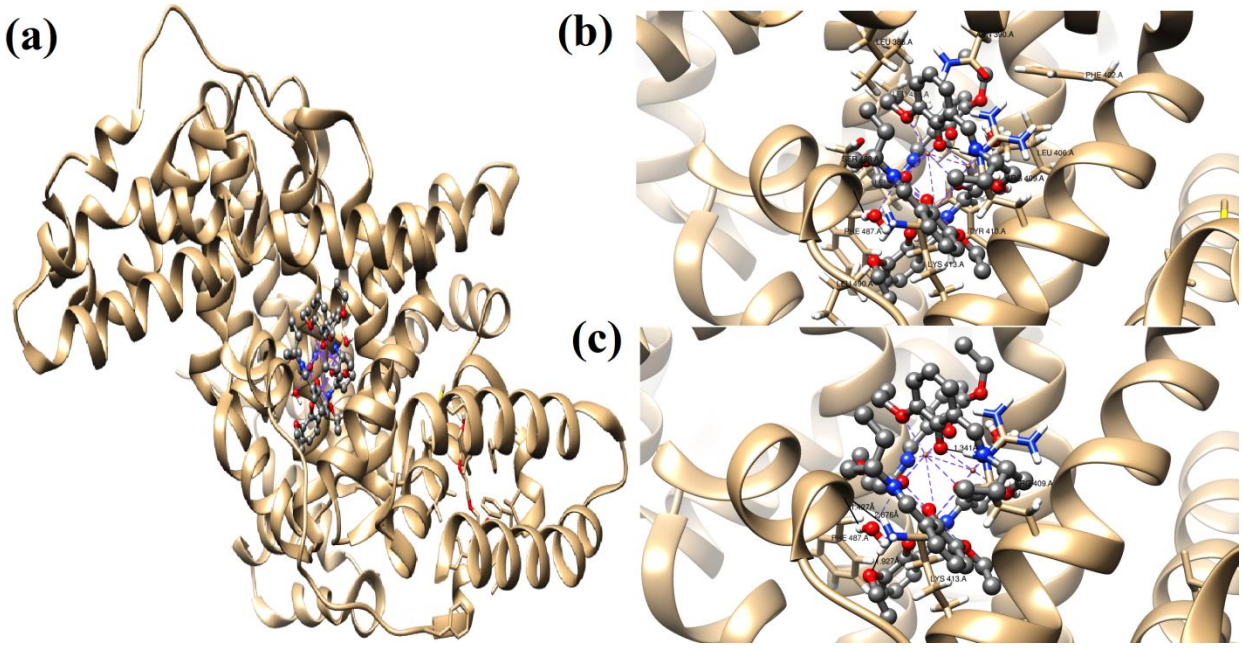

Fig. 4.23 Molecular docking image of complex **1** with BSA (binding site: Tyr410); (a) Interaction of **1** with amino acid residues of BSA (b) Zoom view of interaction of **1** with amino acid residues of BSA (c) H-bonding interaction of **1** with amino acid residues of BSA.

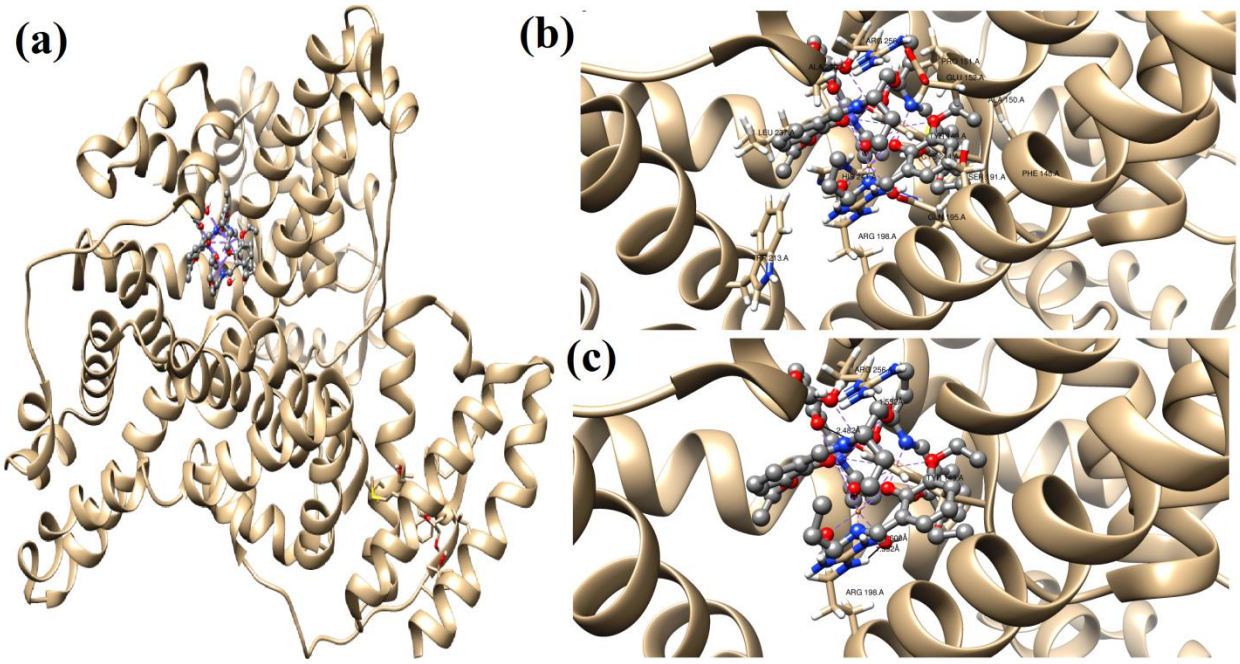

Fig. 4.24 Molecular docking image of complex **2** with BSA (binding site: Tyr410); (a) Interaction of **2** with amino acid residues of BSA (b) Zoom view of interaction of **2** with amino acid residues of BSA (c) H-bonding interaction of **2** with amino acid residues of BSA.

Table 4.11 Docking Chimera fitness docking scores of the copper(II) complexes with BSA and HSA.

Pose	**Chimera score**			
	Complex 1		**Complex 2**	
BSA				
Binding sites				
	Tyr 149	*Tyr 410*	*Tyr 149*	*Tyr 410*
1	281.8	185.4	270	262.7
HSA				
Binding sites				
	Tyr 150	*Tyr 407*	*Tyr 150*	*Tyr 407*
1	191.4	187.7	158.9	151.5
2	191.7			

Table 4.12 Amino acid residues in BSA/ HSA which interact with complexes.

	Charged amino acids residue		Polar amino acids residue		Hydrophobic amino acids residue	
BSA						
1 (Active site: Tyr149)	Arg256, Arg198,	Glu152, Arg194	Tyr149, Gln195, Trp213, His287	His241, Tyr147, Ser191,	Ala290, Phe148	Val240,
1 (Active site: Tyr410)	Arg409,	Lys413	Tyr410, Asn390	Ser488,	Leu490, Leu452, Leu429, Phe402,	Leu386, Leu406, Leu456, Phe487
2 (Active site: Tyr149)	Arg198, Glu152, Arg217	Arg256, Arg194,	Tyr149, Gln195, Tyr156, Cys252,	His241, Ser191, Cys244, His287	Val240, Pro151, Leu153, Ala150	Phe148, Ala290, Leu237,
2 (Active site: Tyr410)	Arg198, Arg256	Glu152,	Tyr149, His241, Trp213,	Ser191, Gln195, Cys244	Pro151, Val240, Ala290	Ala150, Leu237,
HSA						
1 (Active site: Tyr150)	Lys195, Glu292, Glu153,	Lys199, Arg257, Arg222	Ser192, Gln196, His242,	Trp214, Tyr150, His288	Phe157, Ala191,	Phe149, Ala291
1 (Active site: Tyr407)	Arg484, Arg197	Asp451,	Asn458, Cys477, Ser454	Ser202, Trp214,	Leu198, Leu347, Val455, Val482, Leu481	Ala201, Val344, Leu457, Phe206,
2 (Active site: Tyr150)	Lys199, Glu153, Arg222,	Arg257, Lys195, Glu292	His242, Gln196, His288,	Ser192, Trp214, Tyr150	Ala291, Phe157	Phe211,
2 (Active site: Tyr407)	Arg484, Lys205, Lys199	Arg485, Arg348,	Cys461, Ser202, Trp214, Ser480	Cys477, Asn458, Ser454,	Ala201, Leu481, Val482, Ala210, Leu457,	Val344, Leu198, Phe206, Val455, Leu347

At the binding site complex **1** was surrounded by three hydrophobic amino acid residues (Ala 290, Val 240, Phe 148) involved in hydrophobic interactions, seven polar amino acid residues (Tyr149, His241, Gln195, Tyr147, Trp213, Ser191, His287) and four charged amino acid residues (Arg256, Glu152, Arg198, Arg194) interact by ionic interactions (Table 4.12). One

hydrogen bonding interaction was observed between the complex **1** and Arg198 [N-H (of Arg198) ···N3 (of **1**) = 1.857Å] (Table 4.13). On the other hand, there are seven categories of hydrophobic contacts between **2** and amino acid residues of BSA, including, Val240, Phe148, Pro151, Ala290, Leu153, Leu237 and Ala150. Some polar amino acid residues (Tyr149, His241, Gln195, Ser191, Tyr156, Cys244, Cys252, His287) and some charged amino acid residues (Arg198, Arg256, Glu152, Arg194, Arg217) also present and involved in the binding process (Table 4.12). Three types of hydrogen bonding interactions were observed between the complex **2** and polar amino acid residues Arg198, His241 and Arg256 [N-H (Arg198)···O5 = 2.456 Å, N-H (His241)···O3 = 2.062 Å and N-H (Arg256)···O8 = 2.279 Å] (Table 4.13).

From the results obtained from molecular docking between BSA and complexes show that both the complexes were located in the subdomains I and II of BSA. The binding affinity order of complexes with BSA is **1**>**2**. This result corroborated with the experimentally determined binding constants.

Table 4.13 Hydrogen bond interactions for complexes **1-2** with BSA.

Complex	Bonds formed	D···A (Å)	D-H···A (Å)
1 (Active site: Tyr149)	N-H (Arg198)···N3	2.528	1.857
1 (Active site: Tyr410)	N-H (Arg409)···O1	2.349	1.341
	N-H (Lys413)···O12	2.866	1.927
	O2W-1H2W···O (Phe487)	2.309	1.427
2 (Active site: Tyr149)	N-H (Arg198)···O5	3.464	2.456
	N-H (HIS 241)···O3	2.943	2.062
	N-H (Arg256)···O8	3.064	2.279
2 (Active site: Tyr410)	N-H (Arg198)···O2W	2.218	1.392
	N-H (Arg198)···O2W	2.345	1.600
	N-H (Arg256)···O6	2.297	1.552

Molecular Docking with HSA

In order to investigate effective binding site of HSA, we were performed docking of each complex with two different active sites (*Tyr 150* and *Tyr 407)* individually. Based on chimera score (Table 4.11), it is clear that both complexes **1** and **2** selectively bind with HSA at the site of *Tyr 150.* Binding interactions of the complexes with the RCSB protein are shown in Figs. 4.25 - 4.28. Amino acids which are present nearby of the docked complexes are shown in Table 4.12 and the hydrogen bonding parameters are shown in Table 4.14.

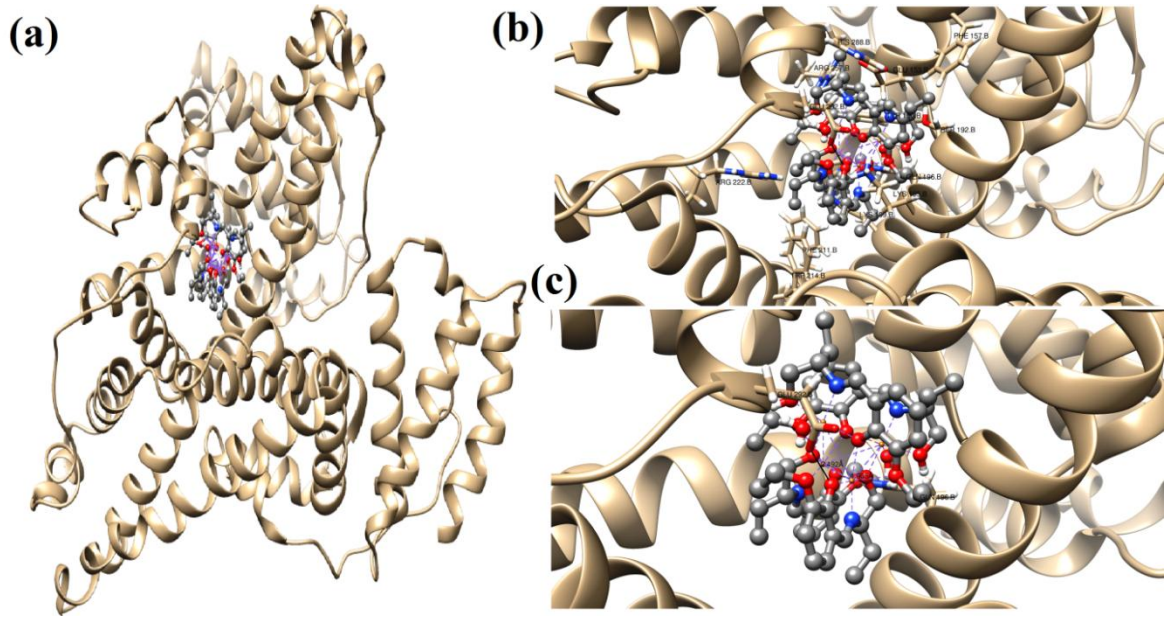

Fig. 4.25 Molecular docking image of complex **2** with HSA (binding site: Tyr150); (a) Interaction of **2** with amino acid residues of HSA (b) Zoom view of interaction of **2** with amino acid residues of HSA (c) H-bonding interaction of **2** with amino acid residues of HSA.

At the binding site complex **1** was surrounded by some hydrophobic amino acid residues (Phe157, Phe149, Ala191, Ala291) involved in hydrophobic interactions, some polar amino acid residues (Ser192, Trp214, Gln196, Tyr150, His242, His288) and also with some charged amino acid residues (Lys195, Lys199, Glu292, Arg257, Glu153, Arg222) interact by ionic interactions (Table 4.12).

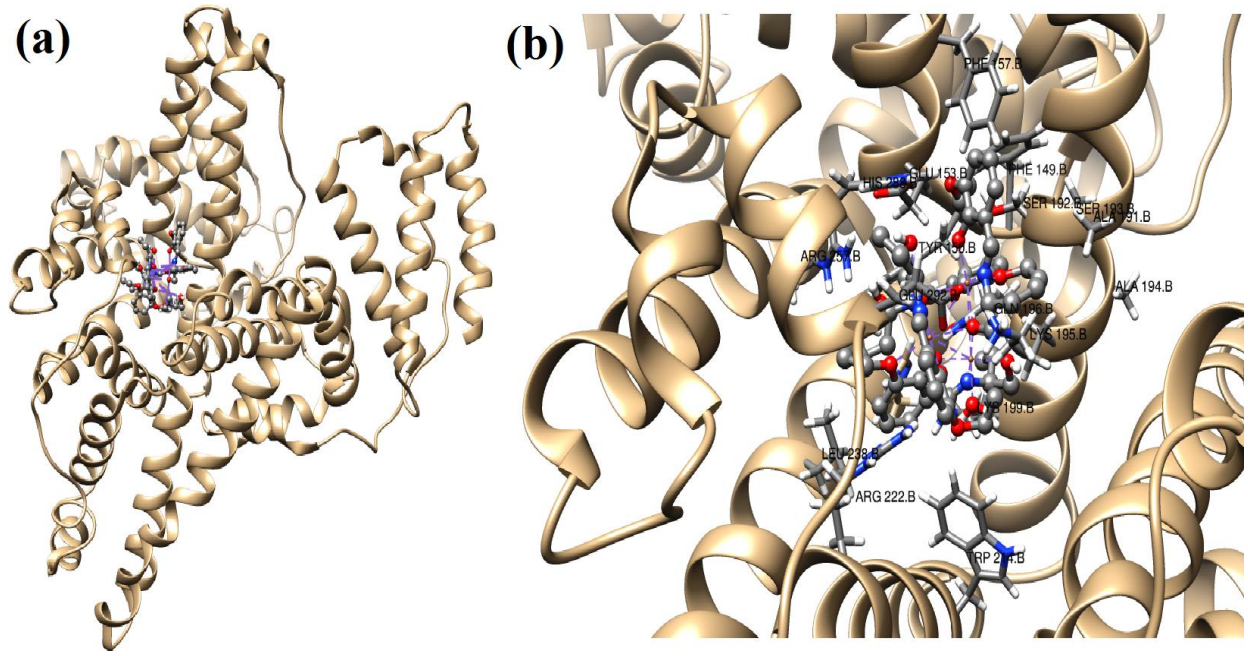

Fig. 4.26 Molecular docking image of complex **1** with HSA (binding site: Tyr150); (a) Interaction of **2** with amino acid residues of HSA (b) Zoom view of interaction of **2** with amino acid residues of HSA.

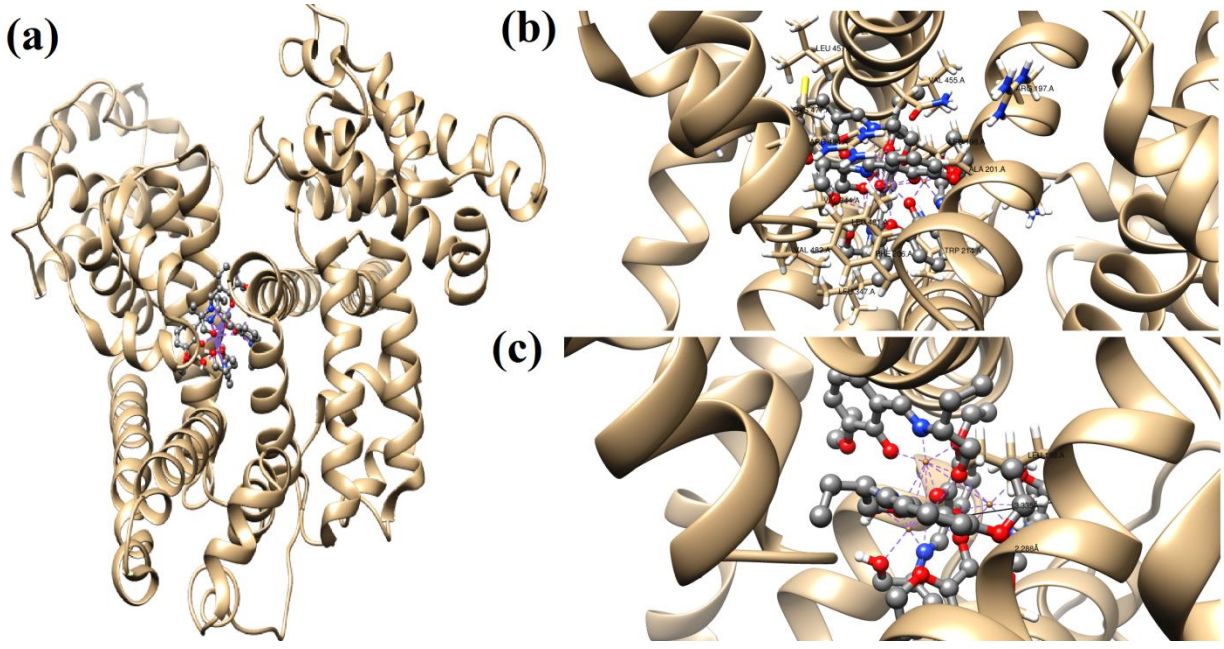

Fig. 4.27 Molecular docking image of complex **1** with HSA (binding site: Tyr407); (a) Interaction of **1** with amino acid residues of HSA (b) Zoom view of interaction of **1** with amino acid residues of HSA (c) H-bonding interaction of **1** with amino acid residues of HSA.

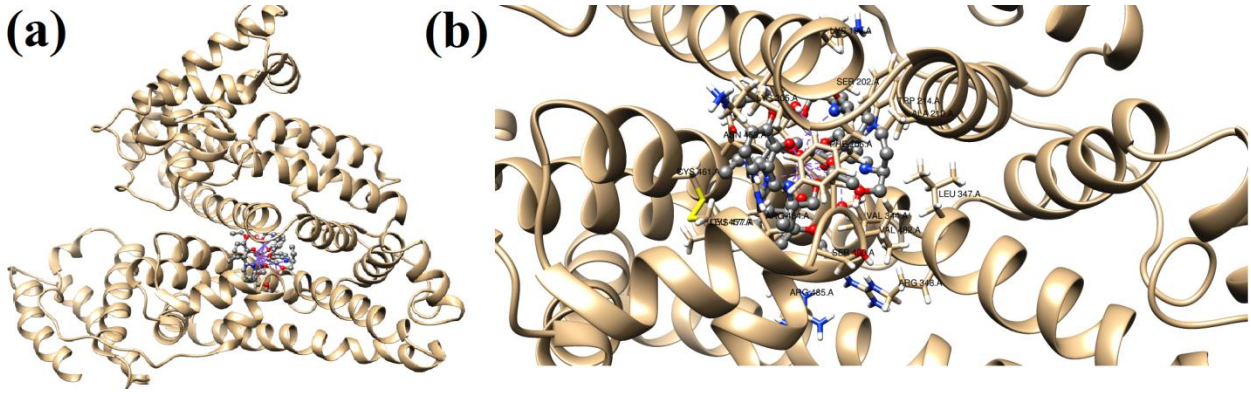

Fig. 4.28 Molecular docking image of complex **2** with HSA (binding site: Tyr407); (a) Interaction of **2** with amino acid residues of HSA (b) Zoom view of interaction of **2** with amino acid residues of HSA.

For interaction with **2**, there are hydrophobic contacts between **2** and some hydrophobic amino acid residues of HSA (Ala291, Phe211, Phe157), some polar amino acid residues (His242, Ser192, Gln196, Trp214, His288, Tyr150) and charged amino acid residues (Lys199, Arg257, Glu153, Lys195, Arg222, Glu292) (Table 4.12). One hydrogen bonding interaction was observed between the complex **2** and amino acid residue Gln196 [N-H (Gln196)···O1 = 1.905 Å] (Table 4.14).

Table 4.14 Hydrogen bond interactions for complexes **1-2** with HSA.

Complex	Bonds formed	D···A (Å)	D-H···A (Å)
1 (Active site: Tyr150)	-	-	-
1 (Active site: Tyr407)	O1W-1H1W···OG (Ser202)	3.048	2.288
2 (Active site: Tyr150)	N-H (Gln196)···O1	2.799	1.905
2 (Active site: Tyr407)	-	-	-

From these results it can be inferred that the complexes **1** and **2** were located in the sub domains I and II of HSA. The molecular docking results also indicate that the binding affinity of complexes is in the order **1**>**2** which corroborate the experimental results.

4.4 Conclusion

In summary, we have presented here the Synthesis, crystal structure, interaction with DNA and protein binding of two tetranuclear (Cu_4) Copper(II) complexes. Single X-ray diffraction analysis evidenced the $\{Cu_4O_4\}$ cubane core of the complexes. Both the complexes have been synthesized using same Schiff base ligand H_2L and results complexes **1** and **2** with different crystal system and different space group, probably due to the presence of different lattice molecules. Both the complexes possess double open cubane core structure. Weak C-H…π interactions results 1D supramolecular architectures for both the complexes. The CT-DNA and protein binding of the compounds were investigated using electronic absorption and emission spectroscopic techniques. Additionally, the molecular docking technique used for establishing the mechanism and mode of action towards DNA and serum albumins theoretically and verified the experimental results. Although many authors have reported the synthesis of tetranuclear cubane complex of Cu(II) but they mainly focused on the magneto-structure correlation of these compounds, the DNA and protein binding studies are quite rare for tetranuclear cubane complexes of Cu(II). A comparison of the kinetic parameters of interactions of reported tetranuclear copper(II) cubane complexes with DNA/SA reveals that complexes **1** and **2** interacts more strongly than the reported compounds (Table 4.9).